Calibrated sea level contribution from the Amundsen Sea sector, West Antarctica, under RCP8.5 and Paris 2C scenarios

Sebastian H. R. Rosier[1,2], G. Hilmar Gudmundsson[1], Adrian Jenkins[1], and Kaitlin A. Naughten[3]

[1]Northumbria University, Newcastle, UK
[2]University of Zurich, Zurich, Switzerland
[3]British Antarctic Survey, Cambridge, UK

Correspondence: Sebastian Rosier (sebastian.rosier@northumbria.ac.uk)

Abstract. The Amundsen Sea region in Antarctica is a critical area for understanding future sea level rise due to its rapidly changing ice dynamics and significant contributions to global ice mass loss. Projections of sea level rise from this region are essential for anticipating the impacts on coastal communities and for developing adaptive strategies in response to climate change. Despite this region being the focus of intensive research over recent years, dynamic ice loss from West Antarctica and

5   in particular the glaciers of the Amundsen Sea represent a major source of uncertainty for global sea level rise projections. In this study, we use ice sheet model simulations to make sea level rise projections to the year 2100 and quantify the associated uncertainty. The model is forced by climate and ocean model simulations for the RCP8.5 and Paris2C scenarios, and is carefully calibrated using measurements from the observational period. We find very similar sea level rise contributions of 19.0 ± 2.2mm and 18.9 ± 2.7mm by 2100 for Paris2C and RCP8.5 scenarios, respectively. A subset of these simulations, extended to 2250,

10 show an increase in the rate of sea level rise contribution and clearer differences between the two scenarios emerge as a result of differences in snow accumulation. Our model simulations include both a cliff-height and hydrofracture driven calving processes and yet we find no evidence of the onset of rapid retreat that might be indicative of a tipping point in any simulations within our modelled timeframe.

1 Introduction

15 The Amundsen Sea region in Antarctica plays a pivotal role in influencing global sea levels, and the dynamics of its glaciers have garnered significant attention in the context of climate change. Since the advent of satellite observations, glaciers in this region, in particular Pine island and Thwaites glaciers, have undergone periods of extensive thinning and retreat, believed to be largely driven by increased ocean melting of their floating ice shelves (Pritchard et al., 2012; Paolo et al., 2015; Gudmundsson et al., 2012; Jenkins et al., 2018). While the region already accounts for a substantial portion of current rates of global sea level

20 rise, vulnerability to unstable retreat might lead to a greatly increased rate of ice loss (Davison et al., 2023; Rosier et al., 2021; Pollard et al., 2015; Feldmann and Levermann, 2015). Modelling challenges, most notably the representation of ocean forcing, model initialisation and the presence of possible future tipping points, mean that there is a wide spread in SLR projections (Robel et al., 2019) and the latest IPCC special report report emphasises the "deep uncertainty" associated with ice sheet model projections (Pörtner et al., 2019).

25   A major challenge in modelling the response of Antarctic glaciers to future emissions scenarios lies in the representation of ocean processes within ice sheet models. Generally, ice sheet modelling studies use simple parameterisations of basal melting, however, this approach cannot hope to capture the complex response of the ocean and ice shelf cavities to atmospheric forcing. In the ASE, increased ice flux through basal melting has not been driven by some simple increasing trend in ambient ocean temperature, but rather intermittent changes in thermocline depth, driven by complex non-local processes, leading to a spatially

30   and temporally heterogeneous response in ice shelf melting (Holland et al., 2022; Jenkins et al., 2018). Increasingly, coupled ice-sheet/ocean models are becoming available that address this shortcoming (e.g. De Rydt and Naughten, 2024; Bett et al., 2024), however these come with a computational cost that makes running large numbers of simulations impractical. This is currently a major downside of the coupled modelling approach, because being able to run a large number of simulations is necessary in order to be able to properly explore the potentially large uncertainty associated with a model prediction.

35   Here, we use an alternative approach by assuming that feedbacks between the ice sheet and ocean are sufficiently small, over the timescales of interest, that we can use standalone ocean model simulations to capture the response of ice shelf cavities to atmospheric forcing. We model melt rates with a 2D plume model that is driven by a stratified water column whose properties in each cavity are obtained from recent state-of-the-art model simulations of the region (Naughten et al., 2023). Both the ocean and ice sheet models are driven by atmospheric forcing from CESM1 for two emissions scenarios: RCP8.5 and Paris2C. We use

40   a comprehensive Bayesian framework to first calibrate our ice sheet model using observations and then evaluate the uncertainty arising from model parameters and internal climate variability, leading to sea level rise projections for the ASE region with corresponding uncertainty estimates.

2   Data and Methods

In order to arrive at our final estimated sea level contribution and calculate the associated uncertainties a number of different

45   modelling components and methods need to come together, These can broadly be divided into two main steps: (1) outputs from a large ensemble of forward model simulations (Úa-*obs*) are compared to observations over the same period to arrive at a likelihood which, given priors for our model parameters, enables us to to calculate posterior probabilities for uncertain model parameters. (2) A second set of model simulations (Úa-*fwd*) use the calculated model parameter distributions to predict changes in ice volume until the year 2100 for different emissions scenarios and quantify the associated uncertainty. Since the

50   forward model simulations are computationally expensive, the uncertainty quantification steps in (1) and (2) are performed on surrogates of the forward model, as described in more detail below. An overview of our methodology is presented in Fig. 1. In the description that follows, we only distinguish between the two sets of forward model simulations where they necessarily differ, e.g. in the model forcing. Where a difference is not stated explicitly, the details are the same. In Section 2.1 we give an overview of the ice-flow model, with a focus on highlighting the uncertain model parameters. These uncertain model

55   parameters, related to ice flow, surface mass balance (SMB), basal mass balance (BMB), calving and model initialisation, are listed in Table 1. Note that parameters related to surface mass balance and calving are not included in the Bayesian calibration
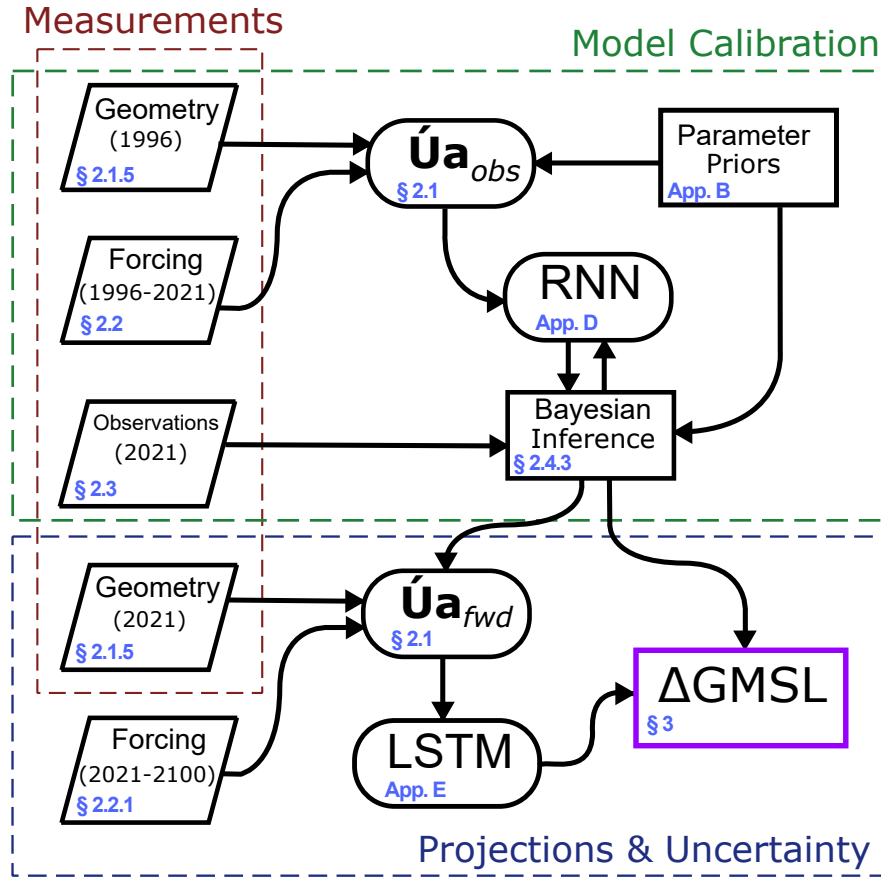
Figure 1. Schematic overview of the inputs, models and processing steps that lead to projections of sea level contribution from the ASE up to the year 2100. We distinguish model calibration steps, resulting in posterior probability distributions for uncertain parameters (dashed green box) from projection/uncertainty steps (dashed blue box). Section or appendices numbers for the relevant step are given in the lower left of each box.

step, as explained in Sec. 2.4 and App. C. Section 2.2 summarises the external forcing for all the simulations, Sec. 2.3 presents the observations used to constrain our model parameters and Sec. 2.4 presents the model calibration methodology.

2.1 Ice flow model

60   All simulations use the Úa community ice-flow model (Gudmundsson, 2020, 2024), which solves the dynamical equations for ice flow with the shallow ice stream approximation (SSTREAM or SSA; Hutter 1983; MacAyeal 1989), using the finite element method on an irregular triangular mesh. The momentum and mass conservation equations are solved simultaneously using a fully implicit forward time integration with respect to both velocities and thickness. Úa uses inverse methods to estimate the uncertain spatial distributions of the rate factor A and the basal slipperiness C, as described in Section 2.1.4. The rate factor

parameter	name	model component	prior mean
m	sliding exponent	ice flow	5
n	creep exponent	ice flow	3.5
p	precipitation factor	SMB	0.077
σ_T	temperature variability	SMB	-0.355
$C_d^{1/2}\Gamma_{TS}$	Stanton number	BMB	1.7×10^{-4}
E_0	plume entrainment	BMB	0.022
$\dot{h}_e$	thickness change error	inversion	3.0
γ_{sC}	C smoothness penalty	inversion	4.0×10^4
γ_{sA}	C prior penalty	inversion	1.6×10^4
γ_{aC}	A smoothness penalty	inversion	8.0
γ_{aA}	A prior penalty	inversion	8.0
C_Q	calving runoff factor	calving	$100\,\mathrm{m}^{-1}\mathrm{yr}^2$

Table 1. Uncertain model parameters included in the Bayesian calibration step described in Section 2.4

65   determines the relationship between the strain rates $\dot{\varepsilon}$ and deviatoric stresses τ through the Glen–Steinemann flow law:

$$\dot{\varepsilon} = A\tau_E^{n-1}\tau \tag{1}$$

where n determines the non-linearity of this constitutive law and we treat as an uncertain model parameter (Millstein et al., 2022). The relationship between basal traction, $\boldsymbol{t}_b$, and basal sliding velocity $\boldsymbol{v}_b$ is given by a mixed Coulomb-Weertman sliding law of the form:

70   $$\boldsymbol{t}_b = \frac{\mu_k N}{\mu_k N + \beta^2\|\boldsymbol{v}_b\|}\beta^2\,\boldsymbol{v}_b\,, \tag{2}$$

where $\beta^2 = C^{-1/m}\|\boldsymbol{v}_b\|^{1/m-1}$, N is the effective pressure, μ_k is the coefficient of friction, and m is an uncertain model parameter. The sliding law (2) is arrived at by setting the basal traction, $\boldsymbol{t}_b$ equal to the reciprocal sum of the Weertman, $\boldsymbol{t}_b^W$ and Coulomb tractions, $\boldsymbol{t}_b^C$ as follows

$$\frac{1}{\|\boldsymbol{t}_b\|} = \frac{1}{\|\boldsymbol{t}_b^W\|} + \frac{1}{\|\boldsymbol{t}_b^C\|}\,, \tag{3}$$

75   where

$$\|\boldsymbol{t}_b^W\| = \beta^2\|\boldsymbol{v}_b\|, \tag{4}$$

$$\|\boldsymbol{t}_b^C\| = \mu_k N\,. \tag{5}$$

This sliding law has been used previously in Barnes and Gudmundsson (2022) and has been implemented in Úa for some time, along other sliding laws.

4

80 We use the simplification that the effective pressure is the difference between ice overburden pressure and water pressure, assuming perfect hydraulic conductivity with the ocean. This results in $N = 0$ zero at the grounding line and N increasing inland as a function of ice thickness. In the limit, as $N \to 0$ basal sliding follows purely Coulomb behaviour, whereas as $N \to \infty$ basal sliding is purely Weertman. The use of a mixed sliding law such as this one has become increasingly popular in recent years due to its flexibility in representing both plastic and hard bed sliding, and an improved representation of conditions

85 near the grounding line.

2.1.1 Surface mass balance

We use a Positive Degree Day (PDD) model to capture two main processes: (1) changes in precipitation resulting from large adjustments of the ice sheet surface elevation and (2) production of runoff that contributes to both surface mass balance and can impact the calving rate (2.1.3). Note that other contributions to changes in precipitation (and hence accumulation) from

90 e.g. temperature changes are already included in the CESM1 climate model that provides our atmospheric forcing, and so these are not included in the PDD model. With this modification, the remaining formulation of our PDD model broadly follows the descriptions given in Huybrechts and de Wolde (1999) and Janssens and Huybrechts (2000). Precipitation (P) is given by

$$P = P_{\text{cesm}} e^{p\Delta T} , \tag{6}$$

where P_{cesm} is the (bias corrected) precipitation forcing from the CESM1 model (Sect. 2.2) and $\Delta T = \gamma_p(s - s_{\text{init}})$ where γ_p

95 is the lapse rate and s_{init} is the initial ice sheet surface elevation. The parameter p captures the expected increase in snowfall arising from the increased moisture content of warmer air, as suggested by climate models (Aschwanden et al., 2019), and is treated as an unknown within our Bayesian framework.

Air temperature is modelled with a normal distribution whose mean is obtained from bias corrected output from CESM1 and standard deviation is given by

100 $$\sigma_M = \sigma_T T_{\text{cesm}} + 1.66, \tag{7}$$

where σ_T is treated as an unknown parameter. This formulation for σ_M was chosen as it has been shown to provide a better fit to observations than using a constant standard deviation (Wake and Marshall, 2015), a result that was confirmed by our own testing. With this simple statistical model of air temperature we can calculate the proportion of precipitation falling as rain, with the remainder therefore falling as snow. This snow accumulates and can be melted as a function of $\gamma_{\text{snow}} PDD$, where

105 PDD is the number of positive degree days and γ_{snow} is the degree day factor for snow. Any meltwater initially percolates down and refreezes as superimposed ice. If the amount of superimposed ice exceeds a threshold, no more superimposed ice is formed and the meltwater contributes to a runoff term. If all the snow is melted, the superimposed ice layer is melted (via a degree day factor for ice γ_{ice}) and finally if that is completely removed the glacier ice itself can be melted, both of which also contribute to a runoff term. Production of runoff is kept track of locally and is subsequently used in our calving law (2.1.3)

110 but we do not model the routing of meltwater across the ice shelf. Our PDD model is updated in monthly time increments in a separate time-stepping scheme to the ice sheet model (whose time steps adaptively change based on convergence).

2.1.2 Basal mass balance

Basal melting or ablation of ice at the base of the ice sheet occurs as a result of transfer of heat from the ocean (on floating ice shelves) and frictional heating where ice is in contact with the bed (i.e. grounded). Ocean induced basal melting accounts for ∼

115 50% of the mass loss of the AIS and is believed to be responsible for much of the measured changes during the observational period, so this component of the model requires particularly careful treatment. Complex feedbacks between ice shelf geometry, cavity circulation, atmospheric forcing and conditions at the domain boundary mean that accurately predicting melt rates is a considerable challenge and generally requires computationally expensive general circulation models, an option that is not feasible for our purposes. Instead, we use an adaptation of the 2D plume model presented by Lazeroms et al. (2018, 2019)

120 and originally proposed by Jenkins (1991, 2011). This retains much more physics than simpler but commonly used depth-dependant parameterisations, while remaining computationally inexpensive to run. A detailed description of our modification to the implementation of Lazeroms et al. (2018, 2019) can be found in App. A and what follows below is only a brief overview introducing the most relevant concepts and parameters.

The plume model considers a two layer system in which an upper layer that is freshened by the addition of meltwater travels

125 along the ice shelf base, driven by a buoyancy difference relative to the ambient ocean layer beneath that has temperature T_a and salinity S_a. The plume itself has temperature T_p, salinity S_p, thickness D_p and velocity U_p and travels in a coordinate system orientated along the ice-shelf base of slope α such that $X = 0$ at the grounding line. The plume equations result from conservation of mass, momentum, heat and salt within the plume and are detailed in Lazeroms et al. (2019). As the plume travels in a positive X direction its volume is increased through entrainment of ambient ocean water ($\dot{e}$) and a meltwater flux

130 at the ice-ocean interface ($\dot{m}$). The entrainment rate is given by

$$\dot{e} = E_0 U_p \sin\alpha \tag{8}$$

where E_0 is an uncertain model parameter. At the ice-ocean interface, melting arises from a balance between turbulent exchange of heat to the ice/ocean interface and latent heat of fusion in the ice:

$$\left(\frac{L}{c}\right)\dot{m} = C_d^{1/2}\Gamma_{TS}U_p(T_p - T_f), \tag{9}$$

135 where L is the latent heat of fusion in ice, c is the specific heat capacity of water and the freezing temperature is a function of the plume salinity and the depth of the ice shelf base

$$T_f = \lambda_1 S_p + \lambda_2 + \lambda_3 b, \tag{10}$$

where λ_1, λ_2 and λ_3 are constant parameters. The thermal Stanton number, $C_d^{1/2}\Gamma_{TS}$ is an uncertain model parameter that plays a key role in determining how effectively warm ocean temperatures can melt the ice-shelf. While the original plume

140 model of Jenkins (1991) solved a system of first order differential equations to obtain the values of U_p and $(T_p - T_f)$ needed to calculate the melt rate, Lazeroms et al. (2019) derived analytical expressions for those variables as a function of distance from the grounding line (detailed in Appendix A2), which we use of in this study.

Beneath grounded ice, we calculate the frictional heating term resulting from basal sliding, which in areas of high basal sliding velocity can become non-negligible. We do not consider any other sources of heat at the bed and calculate melting

145 resulting from this frictional heating as

$$a_b = \frac{\boldsymbol{t}_b \cdot \boldsymbol{v}_b}{\rho L} \tag{11}$$

where $\boldsymbol{t}_b$ and $\boldsymbol{v}_b$ are the basal traction and basal velocity, respectively. The resulting melt rates in the fastest flowing regions are on the order of $1 \, \mathrm{myr}^{-1}$ which is at least two orders of magnitude larger than basal melting due to geothermal heat flux.

2.1.3 Calving Law

150 We allow calving fronts to evolve dynamically during our simulations, using a calving law that depends on a parameterisation of local crevasse depth, as presented in Pollard et al. 2015; DeConto et al. 2021. Total crevasse depth d_{tot} is a sum of terms depending on flow divergence, accumulated strain, ice thickness and surface water. The overall calving rate is given by

$$R_c = 3000 \max[0, \min[1, (r - r_c)/(1 - r_c)]] \tag{12}$$

where $r = d_{tot}/h$ and $r_c = 0.75$, i.e. calving occurs when a crevasse penetrates through 75% of the ice thickness. Our primary

155 motivation here is to include the possibility that a large increase in surface meltwater could lead to hydrofracturing and precipitate the breakup of ice shelves in the region. To this end, we explore the sensitivity of the calving law to the presence of surface meltwater via the parameter C_Q, such that contribution to the total crevasse depth is $f_r C_Q R^2$ (DeConto et al., 2021). Here f_r is a factor that scales from 0 to a maximum of 1 for areas of low to moderate meltwater production (0 to $1.5 \mathrm{myr}^{-1}$). Following DeConto et al. 2021, we use a range for C_Q of 0 to $195 \mathrm{m}^{-1}\mathrm{yr}^{-2}$.

160 In addition to the calving law in Eq. 12, and also following Pollard et al. 2015, we implement structural failure of ice cliffs necessary to allow for the possibility of a MICI driven retreat. The cliff-based calving rate ramps up linearly from zero at a cliff height of 80m to $3 \mathrm{kmyr}^{-1}$ at a cliff height of 100m. Our resulting final calving rate, defined everywhere as a field for the level-set method, is then calculated the maximum of either this cliff-based calving rate or the calving rate given by Eq. 12.

For a calving front to remain fixed, the calving rate must equal the ice velocity normal to the calving front. Generally, for a

165 given calving law, those two quantities are not equal, resulting in migrating calving fronts over time. The Úa model uses the level-set method to solve for this moving boundary problem. The key idea is to introduce a new field variable, $\varphi(x, y, t)$, and define the calving front as the set of points in the (x, y) plane for which $\varphi(x, y, t) = 0$ for any time t. After initial initialisation at the start of the run, the level set function (φ) is evolved by solving the level set equation

$$\partial_t \varphi + F \|\nabla \varphi\| = 0, \tag{13}$$

170 where the scalar F is the speed in outward normal direction, $\hat{\boldsymbol{n}}$, to the calving front, i.e.

$$F = \boldsymbol{v} \cdot \hat{\boldsymbol{n}} - c,$$

where $\boldsymbol{v}$ is the material velocity and c the calving rate. A calving law provides c as a function of some other variables such as cliff height, state of stress, etc., for example as $c = c(f, \sigma)$, where f is the cliff height and σ the Cauchy stress tensor. For the

calving law to be physically admissible, the function f must be frame invariant, a condition that, as shown in (Mitcham and
175 Gudmundsson, 2022), is not satisfied by all previously proposed calving laws.

The implementation details are provided in the Úa Compendium (Gudmundsson, 2024). A similar approach is used in the
Ice-sheet and Sea-level System Model (ISSM), and further technical details for both the ISSM and the Úa ice sheet models,
are provided in Cheng et al. (2023).

2.1.4 Model Initialisation

180 Úa uses the adjoint method to invert for C and A using observed surface ice velocity and the rate of change of ice thickness. It
minimises the cost function $J = I + R$ where

$$R = \frac{1}{2\mathcal{A}} \int \left(\gamma_{sC}^2 \left[\nabla \log_{10}(C/\tilde{C}) \right]^2 + \gamma_{aC}^2 \log_{10}(C/\tilde{C})^2 \right) d\mathcal{A} + \frac{1}{2\mathcal{A}} \int \left(\gamma_{sA}^2 \left[\nabla \log_{10}(A/\tilde{A}) \right]^2 + \gamma_{aA}^2 \log_{10}(A/\tilde{A})^2 \right) d\mathcal{A}$$

(14)

is the regularization term where $\tilde{C}$ and $\tilde{A}$ are priors, $\mathcal{A}$ is the mesh area and $\gamma_{sC}, \gamma_{aC}, \gamma_{sA}, \gamma_{aA}$ are regularization parameters
that determine how much the solution is penalised in terms of smoothness and deviation from the priors and I is the misfit term

185

$$I = \frac{1}{2\mathcal{A}} \int \left([u - u_{obs}]/u_{err} \right) d\mathcal{A} + \frac{1}{2\mathcal{A}} \int \left([v - v_{obs}]/v_{err} \right) d\mathcal{A} + \frac{1}{2\mathcal{A}} \int \left(\left[\dot{h} - \dot{h}_{obs} \right] / \dot{h}_e \right) d\mathcal{A},$$

(15)

where u_{obs}, v_{obs} and $\dot{h}_{obs}$ are observations of surface ice speed and changes in ice thickness and u_{err}, v_{err} and $\dot{h}_e$ are the
observational errors.

By minimising the misfit to both velocities and thickness changes, rather than just velocity (as has generally been done in
190 the past), we can incorporate additional information that helps add further constraints on the inverted A and C fields. However,
these two observational datasets are derived independently and generally not consistent with one another, meaning that our
model will not be able to perfectly fit both the observed velocity and observed thickness change at the same time. A balance
needs to be found such that our model matches both datasets as well as possible. To this end, we take the error terms as given
for the u_{err} and v_{err} but use a spatially uniform $\dot{h}_e$ whose magnitude is one of our uncertain model parameters. The effect
195 of this is that $\dot{h}_e$ becomes a scaling parameter that determines to what degree the inverse procedure tries to match observed
thickness changes as against observed velocities. Details of the observations and errors described above are found in Sec. 2.3.

2.1.5 Ice sheet geometry

To define our ice sheet geometry for the two sets of simulations, we require data for the bedrock elevation (B), surface
elevation (s) and ice thickness (h). We assume that B does not change throughout all our simulations, and here we use gridded
200 data from Bedmachine Antarctica (Morlighem, 2022). The Úa-*fwd* simulations, starting 2021, use the same dataset to define
s and h. Measurements of these fields for the start of the Úa-*obs* simulations are more difficult to obtain and so rather than
using these highly uncertain products, we use a similar methodology to De Rydt et al. 2021. This approach makes use of

the precise measurements by satellite altimeter to work backwards from the present day geometry, subtracting the integrated surface elevation change trend over the period of interest, to calculate the ice sheet surface elevation, s, for 1996. This is fixed initially only for grounded ice that is further than 5 km from the coast in the present day, since altimeter measurements on floating ice are less reliable. With assumptions about flotation and ice density, ice thickness can be solved for given s and B. Therefore, we make use of the position of the 1996 grounding line, for which we use the DinSAR derived grounding line of Rignot et al. 2014a, which approximately corresponds to the period 1992-1996. With this constraint on the extent of freely floating ice for our starting period, we iteratively adjust s where it remains undefined, until the grounding line position of our new geometry matches that 1996 grounding line. We add a regularisation term that penalises large spatial gradients in s, ensuring that $s_{bedmachine} - s_{1996}$ does not vary by large amounts over small spatial scales and a smooth transition between the fixed s field defined by altimetry and the s field that we solve for.

2.1.6 Model Relaxation

Due to shocks in the transient solution immediately after initialization, at least partly caused by insufficient knowledge of bed geometry, all our model runs go through a brief period of relaxation of a few years. The model is initialized, using the inverse methodology outlined in Section 2.1.4 to calculate A and C, and then forced with constant initial mass balance for three years. The model is then re-initialized in an identical manner but with updated ice sheet geometry that arise from the relaxation period. Following re-initialization, the model is run for a further three year spinup with the same constant mass balance term, after which all model forcing terms evolve based on the ERA5 outputs for the period 1996-2021. A three year spinup was chosen as a balance between reducing large spurious thickness changes in the first few years of the simulation while also being as short as possible, and is consistent with Nias et al. (2016).

2.1.7 Adaptive remeshing

We make use of the Úa ice-flow model's adaptive remeshing capabilities, such that the finite element mesh evolves with the changing ice in the domain. For each set of simulations, an initial coarse resolution mesh is generated using mesh2d (Engwirda, 2014) and then immediately refined using nearest vertex bisection. Elements are refined in regions of high strain rate and close to grounding lines and calving fronts. By starting with a coarse initial mesh and refining using this approach, the mesh can both refine and un-refine as, for example, the grounding line migrates inland. Target mesh resolution along the grounding line is 400m and along the calving front is 1500m. Remeshing is done every year and with the same refinement criteria for all simulations.

2.2 Model forcing

Our ice sheet model is forced by changes at both the ocean and atmospheric boundaries. Motivated by the challenges in accurately representing ocean conditions, we drive our ocean melt parameterisation with the aid of recent state-of-the-art ocean model simulations of the region using MITgcm (Naughten et al., 2023). Rather than directly using the melt rates calculated

in this study, which would not be representative of the state of our evolving ice shelf cavity geometry, we use modelled ocean
235   conditions within the three main cavities to force our plume model parameterisation of basal melting. Specifically, we use
thermocline depth together with temperature and salinity averaged above and below the thermocline, resulting in a timeseries
consisting of five variables for each of the three cavities.

The ocean model simulations described above are themselves forced with outputs from the CESM1 model. Results exist
for 5 core scenarios representing different anthropogenic and natural forcing pathways. For our Úa-*obs* simulations, which
240   span 1996-2021, we combine the *historical* scenario (1920-2005) with the RCP4.5 scenario (2005-2080) that most closely
matches observed atmospheric conditions in the model domain. For our Úa-*fwd* simulations we include two scenarios: RCP8.5
and Paris2C, which broadly represent more pessimistic or optimistic scenarios for anthropogenic forcing, respectively. These
scenarios are further divided into 10 ensemble members each, which sample different realizations of internal climate variability
within CESM1. Capturing this variability is important, since is likely to have a strong influence on the region and may have
245   contributed considerably to observed trends (Holland et al., 2019, 2022). Therefore, all of our simulations randomly sample
from these different ensemble members, and the ensemble ID (E_{ID}) is an input to our surrogate model described in Sect.2.4.2
and thus contributes to our uncertainty estimates.

We use the same CESM1 atmospheric forcing as in Naughten et al. (2023) to provide changes in air temperature and
precipitation during the course of our simulations. These two fields then drive the PDD component of our model (Sec.2.1.1),
250   leading to changes in accumulation and surface melting. CESM1 modelled temperature and precipitation exhibit clear and
systematic biases in the region which must be corrected for before they can be used to force the PDD model. Temperature
shows an overall cold bias and differences in seasonal variability, which we correct for using processed data from 14 Automatic
Weather Station (AWS) data in the region (Janet, Kohler Glacier, Noel, Kominko-Slade, Kathie, Ferrigno, Up Thwaites Glacier,
AUstin, Toney Mountain, Lower Thwaites Glacier, Inman Nunatak, Bear Peninsula, Evans Knoll and Backer Island), obtained
255   from the AntAWS Dataset (Wang et al., 2023). We compared CESM1 precipitation in the period 1998-2018 to precipitation
from ERA5 reanalysis (Hersbach et al., 2017) and the MAR regional climate model (Marion et al., 2019; Donat-Magnin et al.,
2020) and modified CESM1 precipitation by a spatially varying scaling factor to minimise the misfit between CESM1 and
these two datasets.

2.2.1   Extended forcing

260   The model forcing described above, derived from climate and ocean modelling, only extends to the year 2100. To model ice
sheet behaviour beyond this point in time, we require some method to extend our model forcing. Many different approaches
could be used here, but our motivation in running these extended simulations stems from the inherently long response times
of the ice sheet to perturbations in climate, and so we aim to reveal a more complete picture of the ice sheet's response to the
climate perturbations imposed in our main set of runs (2021-2100). Thus, in our extended simulations we repeat the forcing
265   from 2080-2100 cyclically, after having removed any linear trend that may be present within this 20 year period. By detrending
the forcing, we keep climate relatively constant to allow the ice sheet more time to adjust to its new state, and furthermore
we avoid large discontinuous jumps in the forcing terms after each 20 year repeat cycle. We prefer to extend our simulations

with a cyclical forcing rather than driving the model with constant conditions in order to preserve potentially important natural variability (Jenkins et al., 2018).

270 ## 2.3 Observations

Key to our uncertainty quantification approach is the use of observations to update our prior estimates of uncertain model parameters. We also require observations to initialise the ice-flow model for simulations starting in 1996 and 2021, as described in Sec. 2.1.4. For both purposes, we use satellite observations of surface ice speed and surface elevation change over the entire ASE region. While satellite products have the significant advantage of providing unparalleled spatial coverage, ascribing a

275 precise date to a particular field is often difficult, since velocity and surface elevation change maps are mosaics made up of many repeat satellite passes. Thus, the simulation start dates of 1996 and 2021 were chosen to ensure that the velocity and surface elevation change data were approximately aligned in time, but the precise timing is not well defined.

Velocity observations for Úa-*obs* (i.e. initialised for 1996) are from the MEaSUREs InSAR data for the Amundsen Sea Embayment (Rignot et al., 2014b). These data originate from the ERS-1 and are dated from the 1st January to the 31st December

280 1996. Details of the error sources and estimation are provided in Mouginot et al. (2012), and the resulting term is the square root of the sum of the independent errors squared. Velocity observations for Úa-*fwd* are from the MEaSUREs annual Antarctic ice velocity map (Mouginot et al., 2017a). These observations are dated from 1st July 2019 to the 30th June 2020 and details of the errors can be found in Mouginot et al. 2017b. The two velocity maps described above are converted to surface ice speed and then differenced to provide one component of our observations with which we calibrate the forward model.

285 Satellite derived $\dot{h}_{obs}$ are obtained from ITS_LIVE, which combines a number of satellite sensor observations from 17th April 1985 to 16th December 2020 (Nilsson et al., 2022; Nilsson and Paolo., 2023). These data are provided as a change in ice sheet elevation relative to December 16 2013, at a monthly resolution. For initialisation of each forward model we use an average of this field in the three years preceding the simulation start date, whereas for model calibration we calculate the difference in ice sheet elevation between 1st January 1996 and 16th December 2020. As described in Sec. 2.1.4, the $\dot{h}_e$ error

290 term is treated as an uncertain model parameter for the purposes of model initialisation. For model calibration, we use the supplied error term, which is a root mean squared error as described in Nilsson et al. (2022).

2.4 Model calibration

The set of Úa-*obs* simulations are used to calibrate our model parameters, assigning probability distributions to these parameters based on how well they fit our observations of the region during the simulation period (1996-2021, Sec. 2.3). Model parameters

295 contributing to uncertainty in our final estimates of sea level rise contribution are listed in Table 1. Nine of these parameters are included in the Bayesian inference step outlined in Sec. 2.4.3. Probabilities for the remaining three parameters, related to SMB (p and σ_T) and calving (C_Q), are specified separately due to there being no sensitivity to these parameters in the present day or over the relatively short observational period, as described in App. C.

2.4.1 Dimensionality reduction

300 Approximating probability distributions for large numbers of parameters and a complex model may require evaluating the forward model sequentially hundreds of thousands of times and the computational cost of our forward model makes this intractable. As an alternative, we use the Úa-*obs* simulations as the training set for a surrogate model that is orders of magnitude faster to run than the forward model and therefore allows proper sampling of the probability distributions. Therefore, we require a surrogate model that takes as input a set of model parameters θ and outputs an expected change in ice speed and surface

305 elevation that we can compare to observations.

Our set of training simulations suffers from the curse of dimensionality, since any model output we are seeking to emulate is defined at every node in the domain, but the information within these simulations is relatively sparse. We use singular value decomposition (SVD) to decompose our set of training simulations into principal components that make use of the strong spatial correlations in the model results. We build an $m \times n$ matrix Y of Úa-*obs* simulation results, where each row is an

310 individual model run y_i in the m member ensemble for a particular combination of model parameters θ_i from the full sample of model parameters Θ, i.e. $y_i = \mathcal{F}(\theta_i)$, each column represents a particular node and y is either the modelled surface elevation change or surface speed change during the course of the simulation. Since all simulations end up with different finite element meshes, the column entries of matrix Y arise from mapping model results to a single finite element mesh, consisting of n nodes, using the underlying shape functions. SVD involves finding the matrices U, S and V such that

315
$$Y = USV^T, \tag{16}$$

where the columns of U and V are the left and right singular vectors and they are both orthogonal such that $U^T U = V^T V = I$. S is a diagonal matrix where the diagonal entries are the singular values of Y and are ordered from largest to smallest. We define the matrix $B = US$ which represents the new basis and each row of B represents the main modes of change between model simulations. The first four rows of B are plotted for Y_{sec} and Y_{vel} in Figure 2. By using only the first k columns of these

320 matrices, we end up with a truncated SVD. The proportion of total variance captured for a given integer k is

$$f(k) = 1 - \frac{\sum_{i=1}^{k} S_{ii}}{\sum_{i=1}^{m} S_{ii}} \tag{17}$$

and for each of the two Y matrices we choose k such that $f(k)>K$, where K is a hyperparameter as described in Sec.2.4.2. This results in an approximation for Y, given by $\tilde{Y} = \tilde{B}\tilde{V}^T$, where $\tilde{B}$ and $\tilde{V}$ contain the first k rows of B and V.

In order to conduct our Bayesian inference in this newly defined framework, we need a way to project fields defined on

325 our finite element mesh into the reduced k dimensional space. Premultipling by $\tilde{B}^T$, followed by $(\tilde{B}^T \tilde{B})^{-1}$ yields the desired mapping from n-dimensional field y to the k-dimensional field $\hat{y}$

$$(\tilde{B}^T \tilde{B})^{-1} \tilde{B}^T y = \hat{y}. \tag{18}$$

2.4.2 Surrogate model

The SVD methodology outlined above provides a way to drastically reduce the dimensionality of our problem by encapsulating

330 each model simulation as a linear combination of $\tilde{B}$ and $\tilde{V}^T$. The matrix $\tilde{B}$ represents the main modes of changed as exhibited
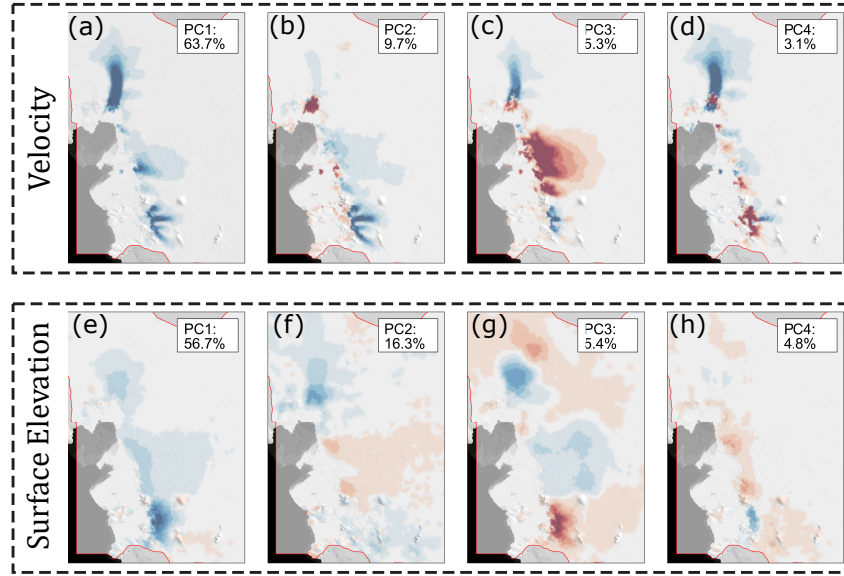
Figure 2. First four principal components for surface ice speed (top row) and surface elevation change (bottom row). The percent of the total variance captured by each component is given in the top right corner of each panel. Background image is from the MODIS mosaic of Antarctica 2008-2009 (Haran, 2014).

in the set of training simulations in Y, and each row of $\tilde{V}^T$ represents the proportion of each of these k components for a particular set of model parameters. Since all our Bayesian inference is done in principal component space, our surrogate model is trained so that, for a particular combination of θ, it can accurately predict the corresponding row of $\tilde{V}^T$ for both speed and surface elevation change (simultaneously). Outside of the existing simulations in Úa-*obs*, we do not know this mapping a-priori. Thus, the input data used to train our surrogate model consists of the matrix of sampled model parameters Θ and the network targets are the corresponding rows of $\tilde{V}^T$. Following a similar approach to Brinkerhoff et al. (2021), we train a deep residual neural network for this purpose. A detailed description of the design and training of this surrogate model can be found in App. D. Once trained, the computationally efficient surrogate model can be used in combination with our parameter priors for Bayesian inference, as described in Sec. 2.4.3.

Before moving forwards with the Bayesian inference, we must verify that the truncated SVD and the surrogate model (reprojected back to model space using the SVD) are able to properly represent the observations. It is entirely possible, if there are no model simulations in Y that show similarities to the observations, that there does not exist a k-dimensional $\hat{y}$ that matches closely to the observations. Similarly, although the surrogate model is trained to agree well with the forward model across the parameter space, there is no guarantee that the output of the model for the optimal set of model parameters agrees well with observations. To veryify these two points, in Fig. 3 we compare the observations of change in surface elevation and surface
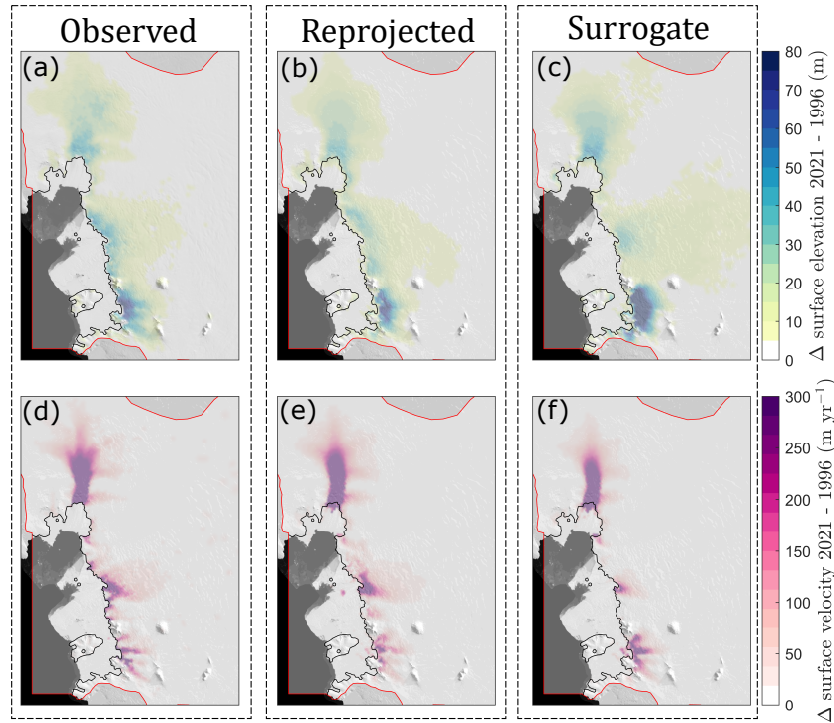
Figure 3. Comparison between observed (left column), reprojected via truncated SVD (middle column) and surrogate (right column) ice surface speed (top row) and surface elevation change (bottom row). Background image is from the MODIS mosaic of Antarctica 2008-2009 (Haran, 2014).

ice speed with their equivalents, having been reprojected using the truncated SVD, and with the surrogate model output for the maximum a posteriori parameters (as described further below). This confirms that both the magnitude and spatial distribution of thinnning and acceleration in the region are well approximated using the truncated SVD and our surrogate model.

2.4.3 Bayesian inference

350 We assume that within the complete parameter space Θ^*, there exists a combination of parameters θ' that leads to a good agreement between model output $\mathcal{G}(\theta')$ and our chosen set of observations in the basis representation $\hat{y}$ (note that $\Theta \subset \Theta^*$ and presumably $\theta' \nsubseteq \Theta$). Our search for θ' and its associated uncertainty is complicated by the presence of noise in the observational data and errors in our forward model. We use a Bayesian framework to infer probability distributions for our model parameters by updating our prior beliefs with observations to obtain a posterior probability. Using Bayes theorem, we can express this
355 posterior probability of certain model parameters given the observations as

$$\pi(\theta \mid y) = \pi(\theta) \cdot \mathcal{L}(y \mid \theta) \tag{19}$$

14

where $\pi(\theta)$ is the prior probability for θ and $\mathcal{L}$ is the likelihood function. The choice of priors is an important step in any Bayesian analysis, and a more detailed description is given in Appendix B. For model parameters that do not have a directly measurable impact within our model, we choose uniform priors bounded by upper and lower limits chosen to span physically plausible values. For parameters related to the surface and basal mass balance models which calculate measurable quantities independently from the ice flow model we use priors constrained on those observations.

The output of our surrogate model $\mathcal{G}$ is related to the observed changes in the basis representation by

$$\hat{\mathbf{y}} + \mathbf{e}_{obs} = \mathcal{G}(\theta) + \mathbf{e}_{model} \tag{20}$$

where $\mathbf{e}_{obs}$ and $\mathbf{e}_{model}$ are the measurement and model discrepancy terms, respectively. Furthermore, the error of our forward model can be broken down into two terms, i.e. $\mathbf{e}_{model} = \mathbf{e}_{Ua} + \mathbf{e}_{rnn}$, which are the errors in the forward ice sheet model and the discrepancy between the forward model and the surrogate model, respectively. We assume that the three discrepancy terms ($\mathbf{e}_{obs}, \mathbf{e}_{Ua}$ and $\mathbf{e}_{rnn}$) are statistically independent and Gaussian distributed and we require an expression for the covariance matrix for each of these terms.

Observational errors are assumed to be uncorrelated, i.e. $\mathbf{e}_{obs} \sim \mathcal{N}(0, \boldsymbol{\sigma}^2_{\boldsymbol{obs}}\mathbf{I})$, where $\mathbf{I}$ is the identity matrix. Observations of surface elevation change and speed are derived from satellite measurements and processing of these data includes (spatially varying) estimates of uncertainty. These supplied error estimates are derived from various sources including instrumental accuracy and the number of data points in a particular grid cell.

We can generally expect errors in the ice sheet model to be spatially correlated, since if the model is not able to accurately capture ice flow at a given node it is likely that the neighbouring nodes will also be similarly inaccurate. Thus, the discrepancy covariance will not be diagonal and so $\mathbf{e}_{Ua} \sim \mathcal{N}(0, \boldsymbol{\Sigma}_{Ua})$. We use an exponential covariance function to represent the spatial correlation in $\boldsymbol{\Sigma}_{Ua}$, i.e.

$$\boldsymbol{\Sigma}_{Ua} = \sigma^2_{Ua}\exp\left(-\frac{\|x_i - x_j\|^2}{2\ell^2}\right) \tag{21}$$

where ℓ is a length scale and σ^2_{Ua} is the model discrepancy variance. This variance term, representing how well the model is able to match observations, is hard to quantify but one reasonable argument is that we are not able to model the ice sheet more accurately than we can observe it, i.e. $\sigma^2_{Ua} > \boldsymbol{\sigma}^2_{\boldsymbol{obs}}$. Here, we conservatively set the model discrepancy variance to be four times the mean observational error, i.e. $200\,\mathrm{m\,yr^{-1}}$ in surface ice speed and $20\,\mathrm{m\,yr^{-1}}$ in dh/dt. We can estimate the model error correlation length scale ℓ by fitting an exponential semi variogram to the model results, whereby the range of the semi variogram is equivalent to ℓ in Eq.21.

Finally, the discrepancy between the ice sheet model and its surrogate can be estimated directly using the test set, hidden from the network during training. In this case, since the network is making a prediction in the reduced k-dimensional space and each component is orthogonal, we can expect these to be spatially uncorrelated and thus $\mathbf{e}_{rnn} \sim \mathcal{N}(0, \boldsymbol{\sigma}^2_{\boldsymbol{rnn}}\mathbf{I})$. With these assumptions,

$$\boldsymbol{\sigma}^2_{\boldsymbol{rnn}} = \frac{\sum_{i=1}^{n_{test}} \left(\mathcal{F}(\theta_i) - \mathcal{G}(\theta_i)\right)^2}{n_{test} - 1} \tag{22}$$

15

where n_{test} is the number of simulations in the test set (566).

390   Importantly, the ice sheet model model and observation discrepancy terms defined above are defined in model space, whereas the surrogate model discrepancy is defined in the reduced k-dimensional space. Thus the final total covariance matrix, defined in the reduced k-dimensional space, is given by

$$\hat{\mathbf{\Sigma}} = A\left(\sigma_{\mathbf{obs}}^{2}\mathbf{I} + \mathbf{\Sigma_{Ua}}\right)A^{T} + \sigma_{rnn}^{2}\mathbf{I} \tag{23}$$

where $A = (\tilde{B}^{T}\tilde{B})^{-1}\tilde{B}^{T}$ follows from Eq. 18. With this estimate of the covariance matrix, we can calculate the likelihood
395   term in Eq. 19, which is given by

$$\mathcal{L} = \prod_{i=1}^{N}\frac{1}{\sqrt{(2\pi)^{N_{out}}\det(\hat{\mathbf{\Sigma}})}}\exp\left(-\frac{1}{2}\left(\hat{y}_{i} - \mathcal{G}(\theta)\right)^{T}\hat{\mathbf{\Sigma}}^{-1}\left(\hat{y}_{i} - \mathcal{G}(\theta)\right)\right). \tag{24}$$

In practice, the posterior probability given in Eq.19 does not have a tractable closed-form solution for such a complex model, so we use a Markov-Chain Monte Carlo (MCMC) algorithm to approximate its form numerically. For this we use UQLab (Marelli and Sudret, 2014), which provides an extensive suite of uncertainty quantification tools for use within MAT-
400   LAB. MCMC algorithms construct a Markov chain that explores the parameter space, whereby a 'chain' is a particular set of parameters in a given iteration. In each iteration, a new set of parameters is proposed in each chain and these are either accepted or rejected. After a sufficient number of iterations, the Markov chain converges such that the distribution of samples closely approximates the true posterior distribution. We used the Affine Invariant Ensemble (AIES) algorithm to determine whether a proposed step for each chain should be accepted, due to its strength in dealing with correlation between parameters
405   and only requiring one tuneable parameter (a, which we set to 1.5). Further details on the AIES algorithm and the choice of a can be found in Goodman and Weare (2010); Allison and Dunkley (2013). We ran the AIES algorithm with 20 chains for 5000 iterations and verified convergence using the Gelman-Rubin diagnostic (Gelman and Rubin, 1992).

Once the Markov chains have converged, we take the final 1000 iterations for each chain and infer the marginal distributions and copula, once again using the uncertainty quantification tools within UQLab. Histograms show the converged samples for
410   each chain, along with the fitted marginals are plotted along the main diagonal of Fig. 4. The off-diagonal elements show the joint probability distribution for each pair of model parameters, helping to reveal correlations between certain model parameters (correlation coefficient between the pairs of parameters is included in the bottom left corner of the upper diagonal panels). Having inferred the probability distributions for each parameter, we use latin hypercube sampling to generate a large sample of model parameters, with which we can run our forward model.

415 3 Sea level rise projections

We run our forward model until 2100, sampling from parameter probability distributions as calculated in Sec. 2.4. Sea level contribution is calculated as change in ice volume above flotation, assuming an area of the ocean of $3.625 \times 10^{14}\mathrm{m}^{2}$, meaning that 1mm of sea level contribution is equivalent to $\sim$362.5Gt of water equivalent ice added to the ocean. Once again, our uncertainty quantification approach requires a large number of forward model evaluations, and so we train a deep surrogate
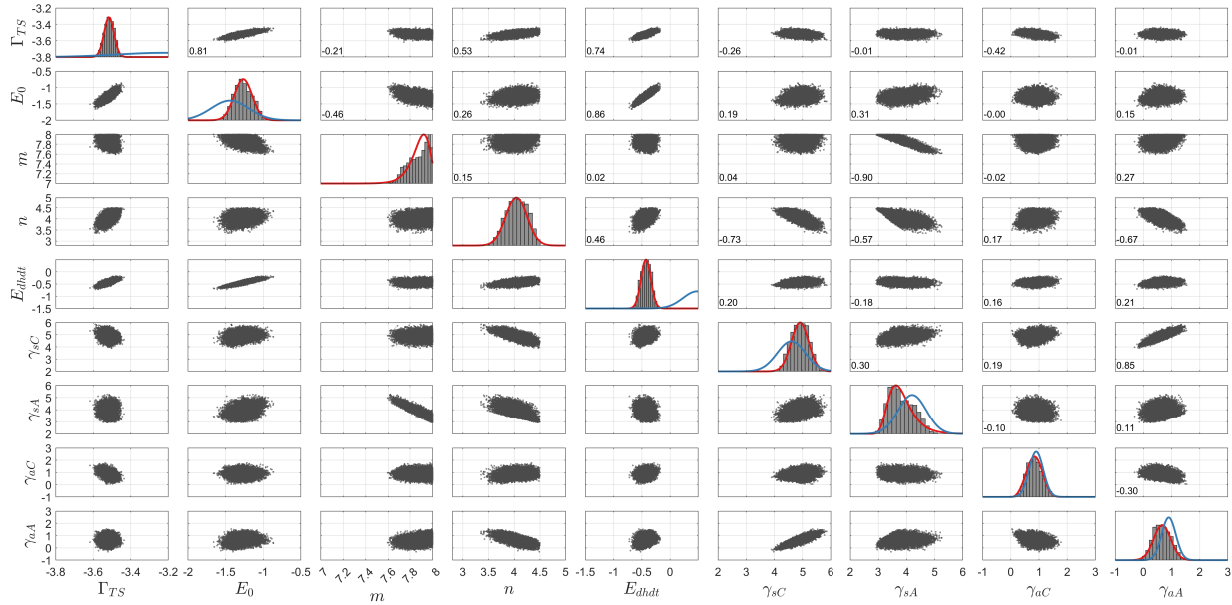
Figure 4. Parameter distributions for each converged chain in the final 1000 iterations of the MCMC algorithm. Red lines in the panels of the main diagonal show the fitted probability distribution for each parameter, blue lines show the priors (not shown if a uniform prior was used). The number in the bottom left corner of the upper diagonal plots shows the correlation coefficient between each two sets of parameters.

model that takes as input a vector of model parameters along with the forcing ensemble ID (E_{ID}) and outputs cumulative change in ice sheet volume above flotation in each modelled year from 2021 to 2100. This is a different surrogate to that described in Sec. 2.4.2 and details of the network architecture, its training and validation can be found in App. E. The surrogate is trained separately to make predictions for the two emissions scenarios, from a training set of ∼2000 simulations with 20% held back for validation and testing. The RMSE between forward model (target) and surrogate (predicted) cumulative change in volume above flotation by the year 2100 was 1.65mm and 1.35mm for the RCP8.5 and paris2C scenarios, respectively. Expressed as a percentage error between targets and predictions, the surrogate model error was 5.7% and 9.5% for Paris2C and RCP8.5, respectively.

Using the surrogate model we calculate a timeseries of sea level contribution until 2100 for one million samples drawn from the posterior parameter probability distributions, allowing for dense sampling of the parameter space and robust estimation of the probability distribution for each year. We show the resulting sea level curves for the RCP85 and Paris 2C scenarios, along with selected confidence intervals, in Fig. 5. This shows that there is almost no difference in sea level contribution by the year 2100 for the two scenarios and the uncertainties are almost identical, although RCP8.5 has a slightly wider range of extremes than Paris 2C. Results from a one million member ensemble of the Paris2C scenario show a median SLR contribution of 19.0±2.2mm from the ASE by 2100, and 18.9±2.7mm for RCP8.5. The 5-95% percentiles (the so-called "very likely
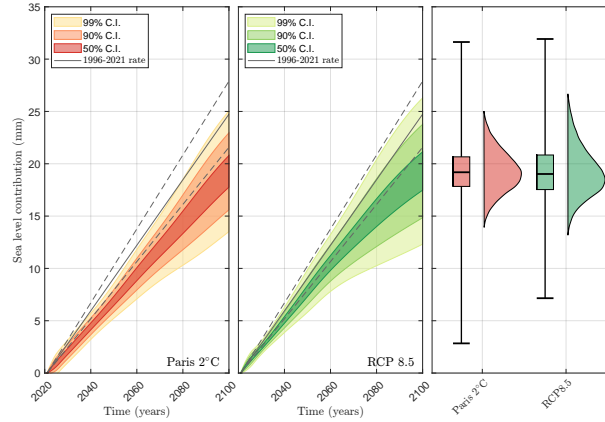
Figure 5. Sea level contribution from the ASE for the Paris 2C and RCP8.5 emissions scenarios, as calculated by the surrogate model. Also plotted is the mean observed 1996-2021 rate for the region (solid black line) and its propagated uncertainty (dashed black lines) as calculated using the input-output method (Davison et al., 2023). Shading indicates the 50, 90 and 99% confidence intervals. Box plots in the right handle panel show the mean, interquartile range and full range of SLR contributions for each emissions scenario.

435 range" in IPCC reports) are 15.6-22.9mm and 15.1-24.0mm for Paris2C and RCP8.5. These projections represent a similar but generally slightly lower estimate than most previous estimates, as discussed in more detail in Sec. 5.

To explore the response of each glacier in more detail we look to the Úa-*fwd* simulations directly, rather than the surrogate model that only provides information on the sea level contribution. In Fig. 6 we show the final grounding line and calving front positions for all simulations in the year 2100, compared to their starting positions in 2021. To generate this plot, the domain

440 is divided into cells and the colormap represents how frequently a grounding line (red) or calving front (green) lies in a given cell as a percentage of all grounding lines or calving fronts, i.e. 10% would mean that a grounding line or calving front was present in this cell for 10% of the total number of simulations. This figure shows extensive calving front retreat across the entire ASE, with an almost complete collapse of the Dotson and Crosson ice shelves and only very small ice shelves remaining in front of Pine Island and Thwaites glaciers. Grounding line movement in the region is generally more limited, with no model

445 simulations finding either significant re-advance or retreat by 2100.

4 Sources of uncertainty

We can explore the relative contribution to total uncertainty arising from different model parameters and internal climate variability using Sobol indices. These are based on the principal that the forward model can be expanded into summands of increasing dimension, such that the total variance is then given by the sum of the variance of these summands. The first-order

450 Sobol indices ($\mathcal{S}_i$) represent the effect that only parameter θ_i has on the variability of the model response (Y), i.e.

$$\mathcal{S}_i = \frac{\text{Var}\left[\mathbb{E}(Y|\theta_i)\right]}{\text{Var}(Y)} \tag{25}$$

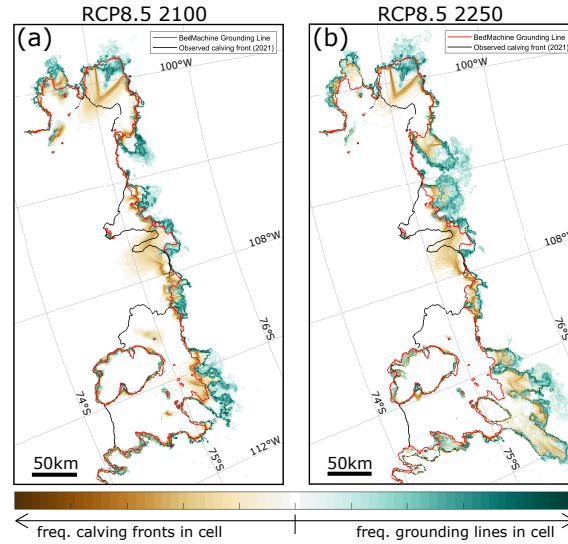**Figure 6.** Grounding line and calving front positions for all Úa-*fwd* simulations (panel a) and Úa-*extended* simulations (panel b) for the RCP8.5 scenario. Locations of the grounding line (red line) and calving front (black line) in 2021 are also shown. Model results are transferred to a uniform grid and the colormap indicates the proportion of simulations for which a grounding line (blue-green colormap) or calving front (brown colormap) is present in a particular grid cell.
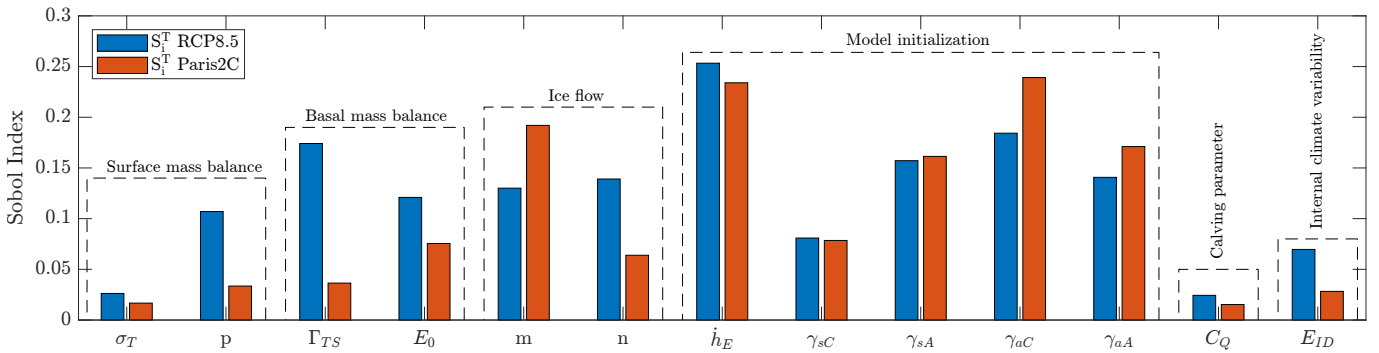

Figure 7. Sobol indices for each model input, representing the fractional contribution of each input on the uncertainty in our projections of sea level contribution for the ASE. Each input consists of two columns, showing the Sobol index as calculated for either the RCP8.5 or Paris 2C scenarios.

Higher order Sobol indices give the interactions between parameters and the total Sobol index for a parameter is then the sum of all Sobol indices. We plot the total Sobol indices for each model input in Fig. 7. The first twelve Sobol indices for each scenario represent parametric uncertainty while E_{ID} represents uncertainty resulting from internal climate variability.

455   Overall, the $\dot{h}_e$ parameter related to our inversion is the single most important for both scenarios, and all inversion parameters together contribute 51% and 66% of total uncertainty for RCP8.5 and Paris2C, respectively. Parameters m and n, related to ice

flow, contribute 17% and 19% while parameters related to basal melting (Γ_{TS} and E_0) contribute 18% and 8% for RCP8.5 and Paris2C respectively.

5 Projections in the context of previous studies

460 A number of previous ice sheet modelling studies have produced sea level rise projection for the Amundsen Sea Embayment. Direct comparison with many of these studies is made challenging since they cover a range of time periods, domains and forcings, however limited comparison helps contextualise the results presented here.

The recent study of Wernecke et al. (2020) is arguably the most similar to ours in terms of methodology, using a combination of model emulation and Bayesian calibration of parameters. For 50 year simulations, the spatially calibrated model ensemble
465 resulted in a median of 16.8mm SLE with 90% confidence intervals of 13.9 and 24.8mm. Several other studies have produced sea level rise projections for the region using a model calibrated using Bayesian methods. In Nias et al. 2019, simulations with a duration of 100 years lead to a median sea level rise contribution of 55.7mm, increasing to 139.7mm after 200 years. Even after calibration, there was significant spread in sea level rise contributions after 200 years, with 5-95th percentiles of 56.2 and 424.3mm, respectively. In another recent study, Bevan et al. 2023 found a median sea level contribution of 16.2mm after 50
470 years, with 5th and 95th percentiles of -0.2 and 39.1mm, respectively.

A number of other studies have explored the future sea level contribution of the ASE region under various climate scenarios, but without the use of Bayesian methods to calibrate their models. Alevropoulos-Borrill et al. (2020) used a subset of CMIP5 simulations to force model simulations of the ASE and found an SLR contribution of between 20 and 45mm by 2100 under RCP8.5. A study including the results of 16 ice sheet model found a median SLR contribution for the ASE of $\sim$20mm by 2100
475 under RCP8.5 scenarios with CMIP5 model forcing (Levermann and others, 2020).

The studies described above cover a wide range of timescales, domains and forcings, but in order to make a rough comparison we convert the results listed above to a time-averaged rate and then average these rates across all studies to arrive at a mean rate of sea level contribution of 0.35mm/yr. Global mean sea levels have risen by 3.7 $\pm$0.5mm yr^{-1} per year in the in the period 2006-2018 (Fox-Kemper and others, 2021). So in the context of the recent observed global rate, this averaged rate represents
480 $\sim$ 10% of the current total. In contrast, in this study we find SLR contribution for RCP8.5 of 0.23mm yr^{-1} between 2021 and 2100, with a 'very likely' range of 0.14-0.30mm yr^{-1}. Thus, our model projections to 2100 result in a median SLR contribution that is at the low end of the range from previous modelling studies of the region.

Our study differs from the studies outlined above in a number of important aspects. Firstly, we explore uncertainty related to a larger number of model parameters (12), including parameters related to calving, initialisation, ice dynamics, basal and
485 surface mass balance. Secondly, using adaptive mesh refinement on an unstructured mesh allows us to use finer resolution at the grounding line (400m in this study). On top of this, by solving velocity and thickness evolution fully implicitly, we expect the simulations presented to provide a more accurate representation of grounding line behaviour. We calibrate our model parameters using observations of changes in both surface elevation and surface ice speed (the model of Bevan et al. 2023 is the only other one to do this for the ASE). Finally, our model simulations also include a dynamically evolving calving

490   front position, rather than a fixed calving front as most previous studies have done. A weakness of our approach is that we
        only include results from one ice sheet model and our forcing is derived from only one climate model, a large component of
        structural uncertainty is not included and would undoubtedly lead to considerably wider confidence intervals than presented
        here. We have also not included in our uncertainty framework any representation of uncertainties in bedrock geometry which
        are also likely to contribute to the overall model spread (Sun et al., 2014). Finally, since we do not use a coupled ice-ocean
495   model, our ocean forcing does not change in response to changes in cavity geometry, a process that could play an important
        role in the evolution of melt rates during our transient simulations (De Rydt and Naughten, 2024).

        Our implementation of the calving laws described in Sect. 2.1.3 is intended to include the possibility of triggering a rapid
        MICI type retreat. Increased runoff on ice shelves can induce an increase in the calving rate through the C_Q parameter and
        parameters related to surface mass balance. If the runoff and calving rate becomes sufficiently large, a rapid 'hydrofracture'
500   driven breakup of the ice shelf could occur, exposing tall ice cliffs which would then rapidly retreat. If this point is reached in
        a simulation, a MICI tipping point is crossed and rapid retreat occurs without the possibility of stopping until the majority of
        the drainage basin is ice free. We include this process to compare our results with those of two modelling studies that find very
        large SLR contributions of over a metre can occur in 125 years or less (DeConto and Pollard, 2016; DeConto et al., 2021).
        Although these projections are for all of Antarctica, a large proportion of the modelled mass loss occurs in the ASE region and
505   these SLR projections are generally considerably greater than other modelling studies. In contrast to the studies of DeConto
        and Pollard 2016; DeConto et al. 2021, we find no evidence that a MICI type retreat occurs in any of our simulations and thus
        including the cliff failure calving criterion has no meaningful impact on our SLR projections. As a result, our SLR projections
        are considerably lower than those of DeConto et al. (2021) for the ASE embayment only, where ∼0.3m of SLRE mass loss
        was modelled by 2200 under a +3°C global warming scenario. This is in spite of the fact that a very large proportion of ice
510   shelf area has been lost in most of our model simulations by 2100 (Fig. 6a), implying that loss of these ice shelves has very
        little affect on future ice loss in the region, as previously shown by Gudmundsson et al. (2023). Note that there are numerous
        differences in our modelling approach compared to DeConto et al. (2021); we do not use the flux formula which is known to
        fail for buttressed ice streams (Reese et al., 2018) and details of the implementation of calving are necessarily different since
        the model presented here uses finite elements and the level-set method.

515   **6 Extended simulations**

        To explore the longer term response of the ASE region to climatic forcing, we conducted extended simulations to the year 2250.
        We randomly selected a total of ∼550 simulations from the Úa-*fwd* model runs and continued them from where they stopped
        in 2100, using the extended forcing described in Sect. 2.2.1. We show the cumulative sea level contribution for the ASE for the
        RCP8.5 and Paris 2C emissions scenarios in Fig. 8a. By 2250 there is a more substantial difference between the two scenarios,
520   with a median sea level contribution of 6.0cm and 7.1cm for RCP 8.5 and Paris 2C, respectively. These results are similar to
        recent modelling work using a calibrated melt rate parameterisation that found a maximum of 8cm of sea level contribution
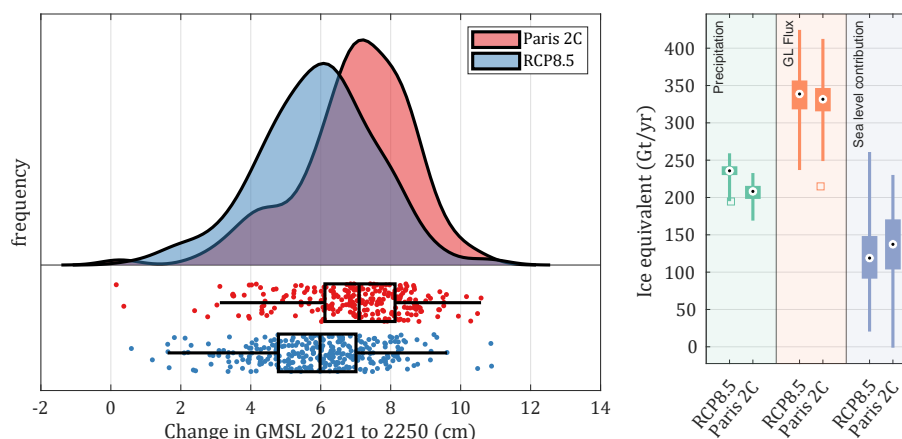
Figure 8. Extended simulation results, showing change in global mean sea level from the ASE region between 2021 and 2250 for the RCP8.5 and Paris 2C emissions scenarios (panel a) and the relative contribution of different ice mass terms for the final year of simulations (panel b).

by 2300 (Reese et al., 2023), but substantially lower than the ~0.3m by 2200 in response to a +3°C global warming scenario (DeConto et al., 2021).

Interestingly, our results show a generally greater sea level contribution under the Paris2C emissions scenario. To explore
525 the reason for this in more detail, we compare the area integrated precipitation, total grounding line flux and change in ice volume above flotation in the final year of these extended simulations. This shows very little difference between scenarios in terms of dynamic ice loss, whereas there is a relatively large difference in terms of total precipitation. These results suggest that over longer timescales increases in precipitation for RCP8.5 may outweigh the relatively minor differences in ocean forcing, relative to the Paris 2C scenario.

530 To better understand how the regional mass loss evolves during the course of our simulations, we plot the rate of volume above flotation loss (or equivalently sea level contribution rate) for all simulations and both scenarios (Fig. 9). In both scenarios, there is a clear increase in the rate of ice loss after 2100, with the rate approximately doubling from 2100 to 2250 in both cases. In addition, a clear difference emerges between the Paris2C and RCP8.5 scenarios up to approximately the year 2100. RCP8.5 shows a substantial decrease in the rate of mass loss that is not present in the Paris2C scenario, but following this both scenarios
535 follow very similar trajectories. By the end of the extended simulations, average annual rates of sea level rise contribution from the ASE reach 0.34 and 0.41 mm/yr for RCP8.5 and Paris 2C, respectively. This represents a similar rate of sea level rise to the observed rate of $0.37 \mathrm{mm\,yr^{-1}}$ obvserved in the period 1996-2021.

7 Conclusions

In this study we conduct calibrated ensemble simulations, with forcing derived from a state-of-the-art ocean model and CESM1,
540 yielding sea level rise projections together with uncertainty estimates for the Amundsen Sea Embayment. We investigate two emissions scenarios: RCP8.5 and Paris 2C, and find the sea level contribution to be almost identical for both scenarios
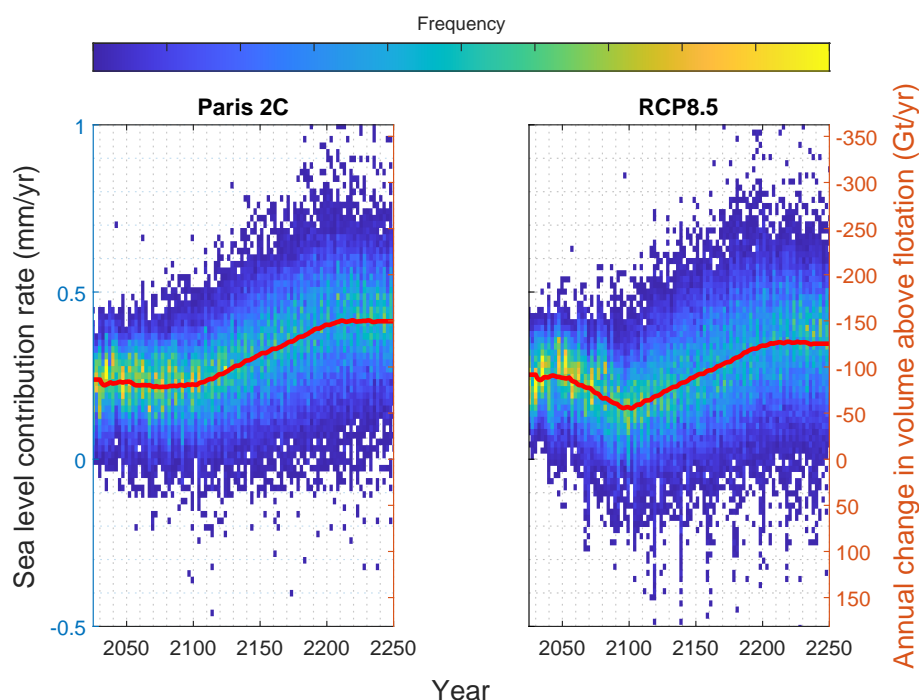
Figure 9. Annual rate of sea level contribution from the Paris2C and RCP8.5 scenarios for all extended simulations. The red line shows the average across all simulations for each scenario, while the background colormap intensity represents how many simulations fall within a particular year/sea level bin.

(19.3mm), although with a slightly higher uncertainty for RCP8.5 versus Paris2C (±2.7mm vs ±2.2mm). These results are generally slightly lower than previously published sea level rise projections for the region. We explore how the sea level contribution of the ASE might evolve further into the future by conducting a subset of extended simulations until 2250. Here,

545 the difference between RCP8.5 and Paris2C is slightly larger (median SLR contributions of 6.0cm vs 7.1cm, respectively), with Paris2C on average leading to a slightly higher sea level contribution as a result of the increased snow accumulation found in RCP8.5.

The similarity in sea level rise contribution between the two emissions scenarios that we investigate is unsurprising, given that the major driver of change in this region is the ocean, and both thermocline depth and temperatures from the ocean model

550 that we use are very similar in both scenarios (Naughten et al., 2023). For both scenarios, we find a large fraction of the total uncertainty comes from parametric uncertainty related to model initialisation. After this, parameters related to ice dynamics and basal melting contribute the most to our calculated uncertainty. Other sources of uncertainty, such as calving and internal climate variability, are relatively small in comparison.

Our model includes the same surface melt and MICI processes as the model of DeConto and Pollard 2016, updated in

555 DeConto et al. 2021. Inclusion of these processes in those studies lead to very substantial and rapid mass loss and these

high-end projections have been the focus of much discussion in the following years. In our simulations, as a result of oceanic melting, calving and increased runoff, the majority of ice shelf area in our simulations is lost by 2100. In spite of this, we find no evidence of a MICI type retreat and in fact the loss of these ice shelves seems to have very little effect on the dynamic mass loss in the region. As a result, our sea level rise projections by the year 2100 are almost an order of magnitude less than those

560 of DeConto et al. 2021 despite using a more pessimistic emissions scenario.

We have not conducted reversibility experiments that would be required to establish whether any of our simulations have crossed a tipping point with regards to ice loss. While we do not see clear evidence of accelerated ice loss towards the end of our simulations, we do not rule out the possibility that Thwaites or Pine Island Glacier may enter a period of self-enhanced retreat leading to far larger sea level contribution beyond the time scale considered here.

565 *Code availability.* The ice flow model Úa, used to drive all model simulations in this study, is fully open-source and available at https://zenodo.org/records/10829346 (Gudmundsson, 2024). Code related to uncertainty quantification and training of the surrogate models is available at https://zenodo.org/records/11922614

Data availability. No new data sets were used in this article.

Appendix A: Plume model description

570 ### A1 Plume routing algorithm

Plume theory was originally conceived to model a system in one horizontal dimension, a situation for which the source of a plume is clear. In order to adapt plume theory to work for two-dimensional models, Lazeroms et al. 2018 incorporated an algorithm that determines the origin of the plume melting each location on an ice shelf. This is important, because melting at a point is not just a function of local conditions, but also the depth at which the plume originates (z_{GL}) and the average slope

575 between the origin and the location being considered (θ_b). Since the work of Lazeroms et al. 2018, further refinements to the plume model parameterisation were described in Burgard et al. 2022, but retaining the original routing algorithm. Here, we describe a modified plume routing algorithm that provides a better fit to melt rate observations in the region, followed by a description of the plume model parameterisation itself.

As a first step, we only calculate ocean-driven melting for nodes considered 'strictly downstream' of a grounding line. This

580 means only for nodes belonging to elements for which no other node is upstream of a grounding line, to avoid ocean-driven melting leaking upstream of the grounding line. For each of these ice shelf nodes, the routing algorithm must determine an origin location for the plume that then drives melting at that point. A list of candidate nodes is generated from all nodes along the main ice sheet grounding line, meaning that plumes cannot originate from pinning points or inland subglacial lakes. For each list of nodes for which a melt rate must be calculated and candidate plume origin nodes, we create an array of x, y and

24

585 z coordinates (where the z coordinate is given by the is draft b for each node), and we refer to these arrays as N_m and N_{GL} respectively. The z coordinate of N_m is then offset by a large negative number and z coordinate of N_{GL} is multiplied by two. Finally, we use a standard k-nearest neighbour algorithm to find the k nearest points in N_{GL} for each point in N_m. The effect of the modifications to the z coordinate is to make deeper candidate nodes in N_{GL} appear closer to nodes in N_m and therefore preferred as plume origin nodes. We choose $k = 10$ for our simulations, leading to 10 candidate plume origin nodes for each
590 node in N_m.

We calculate the depth of the origin plume (z_{GL}) for each melting node as the average ice draft of the k plume origin nodes. The average slope (θ_b) at melting node i is calculated as

$$\theta_{b,i} = \sum_{n=1}^{n=k} \frac{b_i - b_{i,n}}{L_{i,n}}, \tag{A1}$$

where b_i is the ice draft at node i, $b_{i,n}$ is the ice draft at the plume origin node n and $L_{i,n}$ is the horizontal Euclidian distance
595 between node i and plume origin node n.

In addition to the non-local quantities calculated above via the plume routing algorithm, melt rate at each node is a function of local slope (θ_l), ice draft (b), and a depth dependant local temperature and salinity. Vertical profiles of temperature and salinity are generated as a function of ocean model thermocline depth (z_T) and temperature and salinity averaged above (T_s, S_s) and below (T_d, S_d) the thermocline as follows:

$$600 \quad T(z) = \begin{cases} T_s + b\left(\frac{T_d - T_s}{z_T}\right) & \text{if } z \geq z_T \\ T_d & \text{otherwise,} \end{cases} \tag{A2}$$

resulting in a linear variation in temperature (salinity) from the base of the thermocline ($b = z_T$) where $T = T_d$ to the surface ($b = 0$) where $T = T_s$.

Finally, the plume parameterisation requires a mean temperature of water entering the cavity ($\bar{T}$), which is calculated as the weighted average of temperatures in the cavity for each node i.e.

$$605 \quad \bar{T} = \frac{(b - z_T)(T_z + T_d)/2 + (z_T - z_{GL})T_d}{b - z_{GL}}, \tag{A3}$$

where T_z is the local temperature at the ice base $T(z = b)$.

A2 Melt rate calculation

To calculate the melt rate, we implement the plume parameterisation of Lazeroms et al. (2018) in a modified form that partially follows Burgard et al. (2022). We briefly summarise the equations as there are some subtle differences in the definition and use
610 of average properties required by our revised plume routing algorithm (A1).

Using the unmodified Lazeroms et al. (2018) parameterisation the melt rate can be expressed as a function of scaled distance from the grounding line, x':

$$\dot{m} = \left(\frac{C_d^{1/2} \Gamma_{TS}}{L/c} \right) [U' f_U(x')] [\Delta T' f_{\Delta T}(x')] \tag{A4}$$

where the velocity and thermal forcing scales are:

$$615 \quad U' = \left[\frac{\beta_T g E_0 \sin\alpha}{\lambda_3 (C_d + E_0 \sin\alpha)} \right]^{\frac{1}{2}} \left\{ \frac{C_d^{1/2} \Gamma_{TS} \left[\frac{\beta_S}{\beta_T} \left(\frac{S_a c}{L} \right) - 1 \right]}{C_d^{1/2} \Gamma_{TS} \left[1 - \lambda_1 \left(\frac{S_a c}{L} \right) \right] + E_0 \sin\alpha} \right\}^{\frac{1}{2}} (T_a - T_{f,gl}) \tag{A5}$$

$$\Delta T' = \left[\frac{E_0 \sin\alpha}{C_d^{1/2} \Gamma_{TS} \left[1 - \lambda_1 \left(\frac{S_a c}{L} \right) \right] + E_0 \sin\alpha} \right] (T_a - T_{f,gl}) \tag{A6}$$

the dimensionless velocity and thermal forcing functions are given by:

$$f_U(x') = \frac{1}{\sqrt{2}} (1 - x')^{\frac{1}{3}} \left[1 - (1 - x')^{\frac{4}{3}} \right]^{\frac{1}{2}} \tag{A7}$$

$$f_T(x') = \frac{1}{2} \left[3(1 - x) - \frac{1}{(1 - x')^{\frac{1}{3}}} \right] \tag{A8}$$

620   and the scaled distance is defined as:

$$x' = \frac{\lambda_3 (z - z_{gl})}{(T_a - T_{f,gl})} \left\{ 1 + 0.6 \left[\frac{E_0 \sin\alpha}{C_d^{1/2} \Gamma_{TS} \left[1 - \lambda_1 \left(\frac{S_a c}{L} \right) \right] + E_0 \sin\alpha} \right]^{\frac{3}{4}} \right\}^{-1} \tag{A9}$$

In the original derivation of the above equations the ambient ocean properties (T_a, S_a) are considered uniform, while the 1-d ice shelf base shallows monotonically with a constant basal slope ($\sin\alpha$) from its maximum depth at the grounding line depth (z_{GL}). Lazeroms et al. (2018) demonstrated that the parameterisation could be extended to non-uniform slopes simply

625 by using the local value of slope in the above scales, while Burgard et al. (2022) introduced further modifications to account for depth variation in the ambient ocean properties. Here, we follow Lazeroms et al. (2018) in using local slope, expect in the definition of the scaled distance (x'), where we make use of the mean slope defined in A1. In the length scale definition, we further make use of the mean grounding line depth and mean ambient ocean temperature, also defined in A1. We then follow Burgard et al. (2022), in making use of the mean temperature in the expression for $\Delta T'$ and the local temperature to calculate

630 U'. Note that, our plume routing algorithm focuses the origins along deeper parts of the grounding line, unlike the uniform sampling of the cavity inherent in the original algorithm of Lazeroms et al. (2018) that was subsequently used by Burgard et al. (2022). We therefore do not make use of a cavity wide average of either temperature or slope.

Appendix B: Parameter Priors

As a first step to evaluating a posterior probability we require priors for our selected parameters of the Ice Sheet, plume and
635   PDD models (referred to as our three forward sub-models hereafter). One choice would be to use uniform (uninformed) priors,
or to base our priors on some distribution of the parameter choice in previous studies (e.g. Hill et al., 2021). However this
does not take advantage of the extensive observations that exist in the ASE, particularly since the late 1990s when the satellite
record becomes more complete. In the Bayesian framework, these observations can be used to update our probabilistic beliefs.
More specifically, we can calculate the posterior probability for our model parameters, given the observations, and then use
640   this posterior as our prior for the model parameters in the future simulations.

B1   Model inversion priors

Our forward model is initialised using inverse methods so that our simulations agree with observed velocity and surface
elevation changes at their starting date. As described in Sec. 2.1.4, this results in 5 uncertain model parameters related to regu-
larisation of the inverted A and C fields (γ_{aC}, γ_{aA}, γ_{sC} and γ_{sA}) and the relative weighting of the velocity observations versus
645   the surface elevation change observations ($\dot{h}_e$). A standard approach when selecting the magnitude of these regularization pa-
rameters is to conduct an L-curve analysis. The motivation behind this is that there exists a tradeoff between the size of the
regularization term (R, Eq. 14) and how well the resulting model agrees with the data (i.e. the misfit term, I in Eq. 15). By
running the inversion for different amounts of regularization and creating a log-log plot of these two terms, an optimal balance
can be determined as the point of greatest curvature in the plot. We conducted this analysis for the five parameters and the
650   L-curves for each one is plotted in Fig. B1.

To define the prior probability distributions for each inverse model parameter we selected Gaussian distributions whose mean
is the optimal point determined by the L-curve analysis (red points in Fig. B1). It is not possible to attribute a variance based
on the L-curve plots and instead we assign a value such that 99.75% of the distribution falls within one order of magnitude
either side of this mean. This conservative estimate is based on the fact that the L-curve analysis is an ad hoc strategy to tune
655   the regularization parameters and so the most appropriate values may lie some distance away from the points selected by this
method.

B2   Plume model priors

We assign prior probabilities to the two plume model parameters based on how well the plume parameterisation matches with
melt rates as simulated by the MITgcm ocean model simulations of Naughten et al. 2023. This additional Bayesian inference
660   step uses the same framework as described in Sec. 2.4.3 and the posterior probabilities calculated as described in this section
can then be used as prior probabilities for the main model calibration. This ensures that the plume model parameters used in
our forward simulations are broadly consistent with the MITgcm model that drives our ocean forcing while also leading to
changes in ice velocity and surface elevation in the ASE that are consistent with observations. To do this, we must first define
priors for the plume model parameter calibration that follows. We choose Normal distributions whose mean is centered around
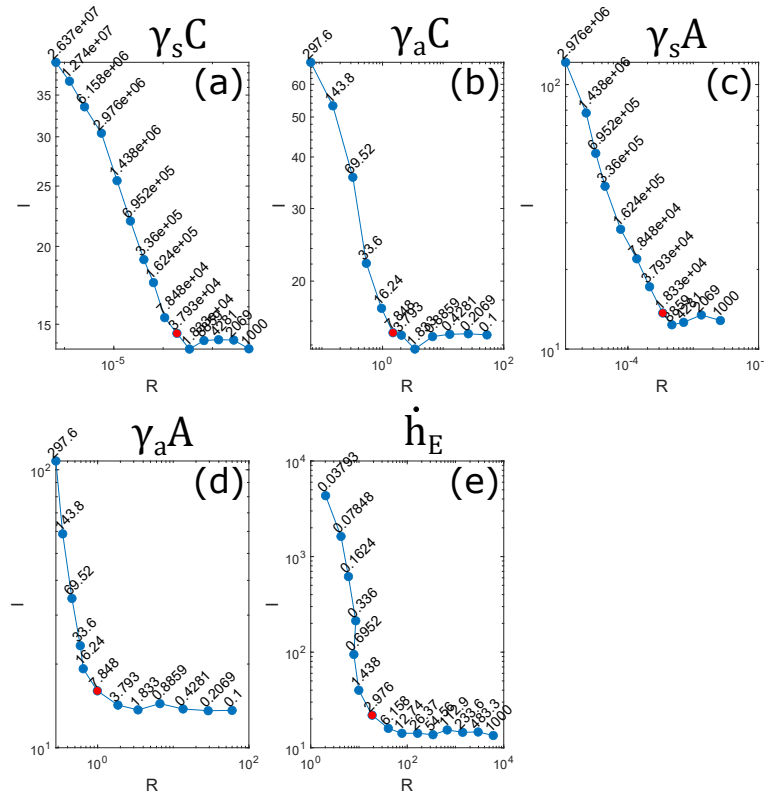
Figure B1. L-curve analysis for model initialisation hyperparameters, showing change in the regularisation term (R, Eq. 14) vs. change in misfit term (I, Eq. 15) for different values of the regularization parameters (where the value of the parameter is given as a label on each point in the plot.

665   the values proposed by (Lazeroms et al., 2018) and with a standard deviation such that 99.7% of the distribution lies within one order of magnitude of the mean.

Since the MITgcm simulations do not include feedbacks on the ice shelf geometry, we run the plume model in a standalone configuration, with the same ice shelf cavity geometry as prescribed in Naughten et al. 2023 and driven by changes in ocean temperature, salinity and stratification provided by the same model. This is done for all model ensemble members and for

670   both the RCP8.5 and Paris 2C scenarios. As outlined in Sec. 2.4.1 and with the same motivation, we greatly reduce the dimensionality of the melt rate fields that we compare by constructing a SVD of the plume model melt rates. We find that a truncation of $k = 10$ enables us to account for $> 95\%$ of the variance in a large ensemble of standalone plume model simulations spanning the parameter space. In this case, however, the standalone plume model is sufficiently computationally efficient that we do not require a surrogate model. Other than this, the calculation of posterior probabilities follows the same procedure

675   as in Sec. 2.4.3, whereby the likelihood is the difference in modelled melt rates in principal component space (Eq. 24). The

maximum a posteriori estimates resulting from this analysis are $\Gamma_{TS} = 1.75 \times 10^{-4}$ and $E_0 = 2.2 \times 10^{-2}$, compared with previously published values of $\Gamma_{TS} = 6.0 \times 10^{-4}$ and $E_0 = 3.6 \times 10^{-2}$, given by Lazeroms et al. 2018.

B3 Ice-flow model priors

We include two ice-flow parameters in our uncertainty analysis; related to the ice rheology (n, Eq. 1) and the basal sliding
680 (m, Eq. 2). Historically, these have typically both been set equal to three but increasingly this paradigm is being challenged. In the case of Pine Island Glacier for, example, two recent studies have found that using a more strongly nonlinear basal sliding parameter is more consistent with observations (Gillet-Chaulet et al., 2016; De Rydt et al., 2021). Similarly, increasing availability and accuracy of remote sensing data along with new methodologies have called into the modelling community's adoption of $n = 3$, with some lines of evidence suggesting a greater sensitivity of ice viscosity to stress is necessary (Millstein
685 et al., 2022; Wang et al., 2022). Despite an increasing amount of research in both these parameters, no clear consensus has emerged on the best choice in either case. For this reason, we choose uniform priors for both, bracketed by upper and lower bounds of $n = 2$ to $n = 5$ and $m = 2$ to $m = 8$. Note that at the upper end of our prior for m, basal sliding becomes effectively plastic.

Appendix C: Un-calibrated model parameters

690 Parameters of the PDD model, whose role is to include changes in surface mass balance under warming scenarios, cannot be readily calibrated on present-day ASE observations where these processes are currently very limited. Similarly, the parameter C_Q controlling the sensitivity of calving rate to surface meltwater is included to introduce the possibility that increased atmospheric warming could lead to accelerated ice shelf collapse but this process has not been observed in the region. Without relevant observations or in absence of sensitivity to these parameters under present-day conditions, assigning posterior
695 probabilities is not possible as it is with the other parameters in Table. 1.

The σ_T parameter of the PDD model largely determines the amount of surface meltwater produced as a result of changes in temperature and thus we can use future simulations of the Regional Atmospheric Model (MAR), that include this process at a point in the future where it becomes relevant, to provide a posterior probability. For this purpose, the PDD model can be decoupled from the ice sheet model, driven by atmospheric forcing and solving for meltwater production with no feedbacks on
700 ice sheet geometry. A recently published modelling study ran the MAR until the year 2100 for the Amundsen Sector, driven by CMIP5 anomalies for the RCP8.5 emissions scenario and found an order of magnitude increase in production of surface meltwater on ice shelves in the region (Donat-Magnin et al., 2021; Marion et al., 2019). By using the same atmospheric forcing as the MAR simulations and comparing meltwater production calculated by the two models in the final twenty years (2080-2100), we can constrain σ_T by finding the value that leads to the best agreement with the state-of-the-art MAR model. Defining
705 the decoupled PDD model as our forward model and the MAR modelled meltwater production as our observations, we can calculate posterior probability using the same framework described in Sec. 2.4.3. We repeated this analysis using $\sigma_M = const$ as a replacement for Eq. 6 but found that this provided a less good fit to the MAR model data.

A different approach is required for the remaining two parameters, p and C_Q, where analogous model simulations in the region that can inform our parameter choices are not readily available. As an alternative, we use published values in the literature to quantify uncertainty. The parameter p, representing the sensitivity of precipitation to changes in air temperature, is widely used within the ice-sheet modelling community and a recently published study by (Nicola et al., 2023) provides an overview of published from a variety of models. We use these values to define a Gaussian prior with mean and standard deviation calculated directly from the spread of previously published values. The parameter C_Q is unique to the recent study by DeConto et al. 2021, who vary this parameter between 0 and $195 m^{-1} yr^2$ and we adopt the same conservative approach, sampling this parameter from a uniform distribution with the same limits.

Appendix D: RNN surrogate

As outlined in Sec. 2.4.2, we require a computationally cheap surrogate model to map from any given θ to a prediction in principal component space ($\tilde{V}^T$) in our Bayesian inference. We choose to use a deep residual neural network as our surrogate model, due to its simplicity and ability to learn complex nonlinear relationships within the training set. Our goal is that, once training is complete, our surrogate model can predict changes in surface ice speed and elevation over the duration of our chosen observational period for a previously unseen combination of model parameters.

As a first step, we define a flexible architecture consisting of an input layer, a series of N residual blocks, and an output layer. Each residual block consists of a series of D sequences of a fully connected layer with H neurons, a batch normalization layer and dropout layer. The output of a residual block is given by the sum of the output of the last dropout layer in the sequence and the its input. In all fully connected layers apart from in the output layer we use swish activation functions. The loss function, defined as the Huber loss between modelled and predicted speed and surface elevation change and reprojected from the reduced SVD representation to the model space, is minimized with the Adagrad optimizer.
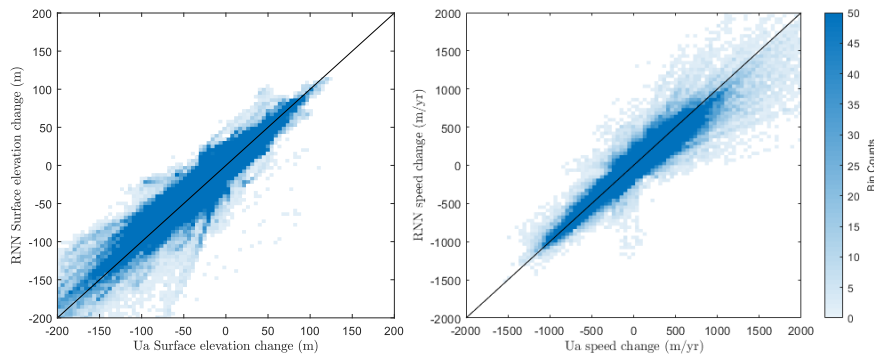

Figure D1. Change in surface elevation and ice surface speed between 1998 and 2021 as predicted by the Úa-*obs* simulations and the RNN surrogate model (2.4.2).

We train this network using a large ensemble of 5670 model simulations with sampled model parameters Θ and modelled surface ice speed and surface elevation change, reprojected using Eq.18. We split our m model simulations into training, validation and test sets with proportions of 70%, 15% and 15%, respectively. The model is built using Tensorflow and network optimization is automated using the Bayesian optimization option in the Keras tuner module to find a learning rate l_R, depth D, number of residual blocks N, number of neurons in each layer H and dropout fraction d that yield the best validation loss. We run this optimization with various choices for K, so that the choice in truncation of the SVD is informed by what results in the best surrogate model. Our final network used $D = 1$, $N = 4$, $H = 115$, $l_R = 0.25$, $d = 0.1$ and $K = 0.9$ (resulting in a trunctation of $k = 8$ for surface elevation change and $k = 11$ for change in speed. Fig. D1 shows the results of the network evaluated on the test set, at every node in the model domain, showing good agreement between the surrogate model and the forward model with an RMSE of $4.77\,\mathrm{m}$ and $35.33\,\mathrm{m\,yr^{-1}}$ for surface elevation and speed change, respectively.

Appendix E: LSTM surrogate

We train a surrogate model to make predictions of sea level rise contribution for a combination of model parameters and forcing ensemble member. Although our primary motivation is to obtain projections for the year 2100, we can make better use of our training simulations by leveraging the inherent time dependency and so the network is trained to make predictions for every year between 2021 and 2100. For this purpose, an Long-short term memory (LSTM) model is appropriate, as it can learn longer time dependencies than a standard recurrent neural network. An LSTM unit consists of three gates that regulate the flow of information in and out of its current state (analogous to the network's memory). Predictions are made sequentially, based on the input to the LSTM and its current state. The first layer of the network is a sequential input layer that takes normalized input parameters from a training subset of the Úa-*fwd* simulations. These are passed to a series of blocks consisting of an LSTM unit and a dropout layer. Finally, a fully connected layer takes the output of the final block and returns a scalar value representing sea level contribution for each time interval that the model is run for. The network loss was calculated using the Huber loss function on the predicted timeseries compared to the result calculated from the Úa-*fwd* simulations. As with the surrogate described in Sec. 2.4.2 we optimized the networks hyperparameters to minimize the validation loss, resulting in a network with 2 blocks of 34 hidden units, a dropout of 0.5, an initial learning rate of 0.007 that was reduced every 10 epochs and a mini batch size of 32. The network was trained separately for the two scenarios (RCP8.5 and Paris2C) using $\sim$800 simulations for each, with a further $\sim$200 reserved for testing and validation. Fig E1 shows the performance of the two trained surrogate models on the test set of each scenario, compared to the outputs from the *fwd* simulations.
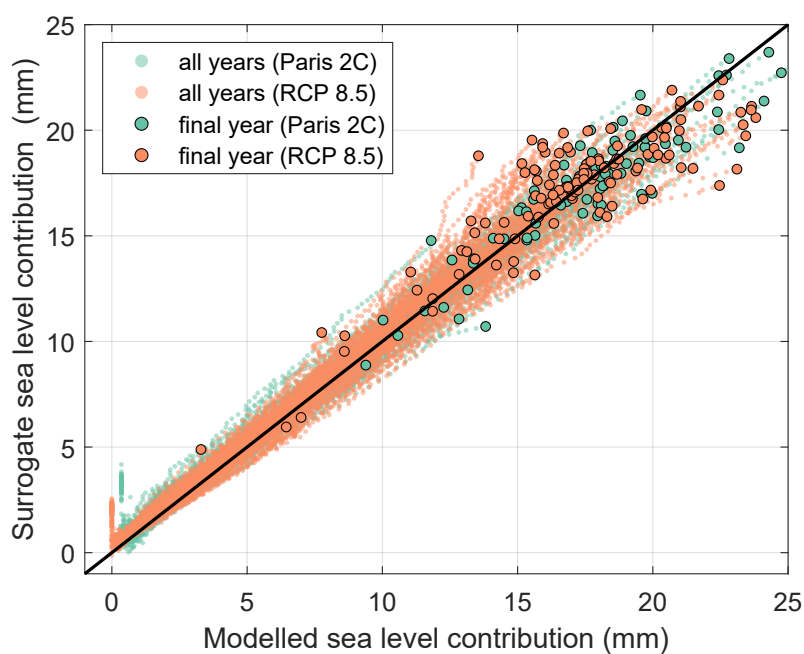
Figure E1. Sea level contribution from the ASE for each year, between 2021-2100, as predicted for the test subset of Úa-*fwd* simulations and the LSTM surrogate model. Prediction for the final year of each simulation, which make up the bulk of our uncertainty quantification and analysis, are highlighted with a black edge.

References

Alevropoulos-Borrill, A. V., Nias, I. J., Payne, A. J., Golledge, N. R., and Bingham, R. J.: Ocean-forced evolution of the Amundsen Sea catchment, West Antarctica, by 2100, The Cryosphere, 14, 1245–1258, https://doi.org/10.5194/tc-14-1245-2020, 2020.

765 Allison, R. and Dunkley, J.: Comparison of Sampling Techniques for Bayesian Parameter Estimation, Monthly Notices of the Royal Astronomical Society, 437, 3918–3928, 2013.

Aschwanden, A., Fahnestock, M. A., Truffer, M., Brinkerhoff, D. J., Hock, R., Khroulev, C., Mottram, R., and Khan, S. A.: Contribution of the Greenland Ice Sheet to sea level over the next millennium, Science Advances, 5, eaav9396, https://doi.org/10.1126/sciadv.aav9396, 2019.

770 Barnes, J. M. and Gudmundsson, G. H.: The predictive power of ice sheet models and the regional sensitivity of ice loss to basal sliding parameterisations: a case study of Pine Island and Thwaites glaciers, West Antarctica, The Cryosphere, 16, 4291–4304, https://doi.org/10.5194/tc-16-4291-2022, 2022.

Bett, D. T., Bradley, A. T., Williams, C. R., Holland, P. R., Arthern, R. J., and Goldberg, D. N.: Coupled ice–ocean interactions during future retreat of West Antarctic ice streams in the Amundsen Sea sector, The Cryosphere, 18, 2653–2675, https://doi.org/10.5194/tc-18-2653-2024, 2024.

775 Bevan, S., Cornford, S., Gilbert, L., Otosaka, I., Martin, D., and Surawy-Stepney, T.: Amundsen Sea Embayment ice-sheet mass-loss predictions to 2050 calibrated using observations of velocity and elevation change, Journal of Glaciology, p. 1–11, https://doi.org/10.1017/jog.2023.57, 2023.

Brinkerhoff, D., Aschwanden, A., and Fahnestock, M.: Constraining subglacial processes from surface velocity observations using surrogate-based Bayesian inference, Journal of Glaciology, 67, 385–403, https://doi.org/10.1017/jog.2020.112, 2021.

780 Burgard, C., Jourdain, N. C., Reese, R., Jenkins, A., and Mathiot, P.: An assessment of basal melt parameterisations for Antarctic ice shelves, The Cryosphere, 16, 4931–4975, https://doi.org/10.5194/tc-16-4931-2022, 2022.

Cheng, G., Morlighem, M., and Gudmundsson, G. H.: Numerical stabilization methods for level-set-based ice front migration, Geosci. Model Dev. Discuss, https://doi.org/10.5194/gmd-2023-194, 2023.

785 Davison, B. J., Hogg, A. E., Rigby, R., and et al.: Sea Level Rise from West Antarctic Mass Loss Significantly Modified by Large Snowfall Anomalies, Nature Communications, 14, 1479, https://doi.org/10.1038/s41467-023-36990-3, 2023.

De Rydt, J. and Naughten, K.: Geometric amplification and suppression of ice-shelf basal melt in West Antarctica, The Cryosphere, 18, 1863–1888, https://doi.org/10.5194/tc-18-1863-2024, 2024.

De Rydt, J., Reese, R., Paolo, F. S., and Gudmundsson, G. H.: Drivers of Pine Island Glacier speed-up between 1996 and 2016, The

790 Cryosphere, 15, 113–132, https://doi.org/10.5194/tc-15-113-2021, 2021.

DeConto, R. M. and Pollard, D.: Contribution of Antarctica to past and future sea-level rise, Nature, 531, 591–597, https://doi.org/10.1038/nature17145, 2016.

DeConto, R. M., Pollard, D., Alley, R. B., et al.: The Paris Climate Agreement and future sea-level rise from Antarctica, Nature, 593, 83–89, https://doi.org/10.1038/s41586-021-03427-0, 2021.

795 Donat-Magnin, M., Jourdain, N. C., Gallée, H., Amory, C., Kittel, C., Fettweis, X., Wille, J. D., Favier, V., Drira, A., and Agosta, C.: Interannual variability of summer surface mass balance and surface melting in the Amundsen sector, West Antarctica, The Cryosphere, 14, 229–249, https://doi.org/10.5194/tc-14-229-2020, 2020.

Donat-Magnin, M., Jourdain, N. C., Kittel, C., Agosta, C., Amory, C., Gallée, H., Krinner, G., and Chekki, M.: Future surface mass balance and surface melt in the Amundsen sector of the West Antarctic Ice Sheet, The Cryosphere, 15, 571–593, https://doi.org/10.5194/tc-15-571-2021, 2021.

800   Feldmann, J. and Levermann, A.: Collapse of the West Antarctic Ice Sheet after local destabilization of the Amundsen Basin, Proceedings of the National Academy of Sciences, 112, 14 191–14 196, https://doi.org/10.1073/pnas.1512482112, 2015.

Fox-Kemper, B. et al.: Ocean, Cryosphere and Sea Level Change, in: Climate Change 2021: The Physical Science Basis. Contribution of Working Group I to the Sixth Assessment Report of the Intergovernmental Panel on Climate Change, edited by Masson-Delmotte, V.,

805   Zhai, P., Pirani, A., Connors, S., Péan, C., Berger, S., Caud, N., Chen, Y., Goldfarb, L., Gomis, M., Huang, M., Leitzell, K., Lonnoy, E., Matthews, J., Maycock, T., Waterfield, T., Yelekçi, O., Yu, R., and Zhou, B., pp. 1211–1362, Cambridge University Press, Cambridge, United Kingdom and New York, NY, USA, 2021.

Gelman, A. and Rubin, D. B.: Inference from Iterative Simulation Using Multiple Sequences, Statistical Science, 7, 457–472, 1992.

Gillet-Chaulet, F., Durand, G., Gagliardini, O., Mosbeux, C., Mouginot, J., Rémy, F., and Ritz, C.: Assimilation of surface velocities acquired

810   between 1996 and 2010 to constrain the form of the basal friction law under Pine Island Glacier, Geophysical Research Letters, 43, 10,311–10,321, https://doi.org/10.1002/2016GL069937, 2016.

Goodman, J. and Weare, J.: Ensemble Samplers with Affine Invariance, Communications in Applied Mathematics and Computational Science, 5, 65–80, 2010.

Gudmundsson, G. H.: GHilmarG/UaSource: Ua2019b (Version v2019b), https://doi.org/https://doi.org/10.5281/zenodo.3706623, 2020.

815   Gudmundsson, G. H., Krug, J., Durand, G., Favier, L., and Gagliardini, O.: The stability of grounding lines on retrograde slopes, The Cryosphere, 6, 1497–1505, https://doi.org/10.5194/tc-6-1497-2012, 2012.

Gudmundsson, G. H., Barnes, J. M., Goldberg, D. N., and Morlighem, M.: Limited Impact of Thwaites Ice Shelf on Future Ice Loss From Antarctica, Geophysical Research Letters, 50, e2023GL102 880, https://doi.org/https://doi.org/10.1029/2023GL102880, e2023GL102880 2023GL102880, 2023.

820   Gudmundsson, H.: GHilmarG/UaSource: Ua2023b, https://doi.org/10.5281/zenodo.10829346, 2024.

Haran, T., B. J. S. T. P. T. . F.: MODIS Mosaic of Antarctica 2008-2009 (MOA2009) Image Map, Version 1, https://doi.org/10.7265/N5KP8037, 2014.

Hersbach, H. B., Berrisford, B., Hirahara, P., Horányi, S., Muñoz-Sabater, A., J. Nicolas, J., Peubey, C., Radu, R., Schepers, D., Simmons, A., Soci, C., Abdalla, S., Abellan, X., Balsamo, G., Bechtold, P., Biavati, G., Bidlot, J., Bonavita, M., De Chiara, G., Dahlgren, P., Dee, D., Dia-

825   mantakis, M., Dragani, R., Flemming, J., Forbes, R., Fuentes, M., Geer, A., Haimberger, L., Healy, S., Hogan, R., Hólm, E., Janisková, M., Keeley, S., Laloyaux, P., Lopez, P., Lupu, C., Radnoti, G., de Rosnay, P., Rozum, I., Vamborg, F., Villaume, S., and Thépaut, J.-N.: Complete ERA5 from 1979: Fifth generation of ECMWF atmospheric reanalyses of the global climate, https://doi.org/10.24381/cds.143582cf, 2017.

Hill, E. A., Rosier, S. H. R., Gudmundsson, G. H., and Collins, M.: Quantifying the potential future contribution to global mean sea level

830   from the Filchner–Ronne basin, Antarctica, The Cryosphere, 15, 4675–4702, https://doi.org/10.5194/tc-15-4675-2021, 2021.

Holland, P., Bracegirdle, T., and Dutrieux, P.: est Antarctic ice loss influenced by internal climate variability and anthropogenic forcing, Nat. Geosci., 12, 718–724, https://doi.org/10.1038/s41561-019-0420-9, 2019.

Holland, P. R., O'Connor, G. K., Bracegirdle, T. J., Dutrieux, P., Naughten, K. A., Steig, E. J., Schneider, D. P., Jenkins, A., and Smith, J. A.: Anthropogenic and internal drivers of wind changes over the Amundsen Sea, West Antarctica, during the 20th and 21st centuries, The

835   Cryosphere, 16, 5085–5105, https://doi.org/10.5194/tc-16-5085-2022, 2022.

Hutter, K.: Theoretical Glaciology: Material Science of Ice and the Mechanics of Glaciers and Ice Sheets, 1983.

Huybrechts, P. and de Wolde, J.: The Dynamic Response of the Greenland and Antarctic Ice Sheets to Multiple-Century Climatic Warming, Journal of Climate, 12, 2169 – 2188, https://doi.org/https://doi.org/10.1175/1520-0442(1999)012<2169:TDROTG>2.0.CO;2, 1999.

Janssens, I. and Huybrechts, P.: The treatment of meltwater retention in mass-balance parameterizations of the Greenland ice sheet, Annals of Glaciology, 31, 133–140, https://doi.org/10.3189/172756400781819941, 2000.

Jenkins, A.: A one-dimensional model of ice shelf-ocean interaction, Journal of Geophysical Research: Oceans, 96, 20 671–20 677, https://doi.org/https://doi.org/10.1029/91JC01842, 1991.

Jenkins, A.: Convection-Driven Melting near the Grounding Lines of Ice Shelves and Tidewater Glaciers, Journal of Physical Oceanography, 41, 2279 – 2294, https://doi.org/https://doi.org/10.1175/JPO-D-11-03.1, 2011.

Jenkins, A., Shoosmith, D., Dutrieux, P., Jacobs, S., Kim, T. W., Lee, S. H., Ha, H. K., and Stammerjohn, S.: West Antarctic Ice Sheet retreat in the Amundsen Sea driven by decadal oceanic variability, Nature Geoscience, 11, 733–738, https://doi.org/10.1038/s41561-018-0207-4, 2018.

Lazeroms, W. M. J., Jenkins, A., Gudmundsson, G. H., and van de Wal, R. S. W.: Modelling present-day basal melt rates for Antarctic ice shelves using a parametrization of buoyant meltwater plumes, The Cryosphere, 12, 49–70, https://doi.org/10.5194/tc-12-49-2018, 2018.

Lazeroms, W. M. J., Jenkins, A., Rienstra, S. W., and van de Wal, R. S. W.: An Analytical Derivation of Ice-Shelf Basal Melt Based on the Dynamics of Meltwater Plumes, Journal of Physical Oceanography, 49, 917 – 939, https://doi.org/10.1175/JPO-D-18-0131.1, 2019.

Levermann, A. et al.: Projecting Antarctica's contribution to future sea level rise from basal ice shelf melt using linear response functions of 16 ice sheet models (LARMIP-2), Earth System Dynamics, 11, 35–76, https://doi.org/10.5194/esd-11-35-2020, 2020.

MacAyeal, D. R.: Large-scale ice flow over a viscous basal sediment: Theory and application to ice stream B, Antarctica, Geophys. Res.-Sol. Ea., 94, 4071–4087, https://doi.org/ttps://doi.org/10.1029/JB094iB04p04071, 1989.

Marelli, S. and Sudret, B.: UQLab: A Framework for Uncertainty Quantification in MATLAB, in: The 2nd International Conference on Vulnerability and Risk Analysis and Management (ICVRAM 2014), pp. 2554–2563, University of Liverpool, United Kingdom, https://doi.org/10.1061/9780784413609.257, 2014.

Marion, D.-M., Nicolas, J., Cécile, A., Hubert, G., Charles, A., Christoph, K., and Xavier, F.: Amundsen Sea MAR simulations forced by ERAinterim, https://doi.org/10.5281/zenodo.4308510, 2019.

Millstein, J. D., Minchew, B. M., and Pegler, S. S.: Ice viscosity is more sensitive to stress than commonly assumed, Commun Earth Environ, 3, https://doi.org/https://doi.org/10.1038/s43247-022-00385-x, 2022.

Mitcham, T. and Gudmundsson, G. H.: On the validity of the stress-flow angle as a metric for ice-shelf stability, Journal of Glaciology, pp. 1–3, https://doi.org/10.1017/jog.2022.25, 2022.

Morlighem, M.: MEaSUREs BedMachine Antarctica, Version 3, https://doi.org/10.5067/FPSU0V1MWUB6, 2022.

Mouginot, J., Rignot, E., and Scheuchl, B.: Mapping of Ice Motion in Antarctica Using Interferometric Synthetic-Aperture Radar Data, Remote Sensing, 4, 2753–2767, https://doi.org/10.3390/rs4092753, 2012.

Mouginot, J., Scheuchl, B., and Rignot, E.: MEaSUREs Annual Antarctic Ice Velocity Maps 2005-2017, Version 1, [Version 1.1] Boulder, Colorado USA. NASA National Snow and Ice Data Center Distributed Active Archive Center, https://doi.org/10.5067/9T4EPQXTJYW9, updated 2022, 2017a.

Mouginot, J. et al.: Comprehensive Annual Ice Sheet Velocity Mapping Using Landsat-8, Sentinel-1, and RADARSAT-2 Data, Remote Sensing, 9, 364, https://doi.org/10.3390/rs9040364, 2017b.

Naughten, K. A., Holland, P., and De Rydt, J.: Unavoidable future increase in West Antarctic ice-shelf melting over the twenty-first century, Nat. Clim. Chang., 14, https://doi.org/10.1038/s41558-023-01818-x, 2023.

875 Nias, I. J., Cornford, S. L., and Payne, A. J.: Contrasting the modelled sensitivity of the Amundsen Sea Embayment ice streams, Journal of Glaciology, 62, 552–562, https://doi.org/10.1017/jog.2016.40, 2016.

Nias, I. J., Cornford, S. L., Edwards, T. L., Gourmelen, N., and Payne, A. J.: Assessing Uncertainty in the Dynamical Ice Response to Ocean Warming in the Amundsen Sea Embayment, West Antarctica, Geophysical Research Letters, 46, 11 253–11 260, https://doi.org/10.1029/2019GL084941, 2019.

880 Nicola, L., Notz, D., and Winkelmann, R.: Revisiting temperature sensitivity: how does Antarctic precipitation change with temperature?, The Cryosphere, 17, 2563–2583, https://doi.org/10.5194/tc-17-2563-2023, 2023.

Nilsson, J., A. G. and Paolo., F. S.: MEaSUREs $ITS_{LIVE}AntarcticGroundedIceSheetElevationChange, Version 1, https://doi.org/10.5067/L3LSVDZS15ZV, 2023$.

Nilsson, J., Gardner, A. S., and Paolo, F. S.: Elevation change of the Antarctic Ice Sheet: 1985 to 2020, Earth System Science Data, 14, 3573–3598, https://doi.org/10.5194/essd-14-3573-2022, 2022.

Paolo, F. S., Fricker, H. A., and Padman, L.: Volume loss from Antarctic ice shelves is accelerating, Science, 348, 327–331,
885 https://doi.org/10.1126/science.aaa0940, 2015.

Pollard, D., DeConto, R. M., and Alley, R. B.: Potential Antarctic Ice Sheet retreat driven by hydrofracturing and ice cliff failure, Earth and Planetary Science Letters, 412, 112–121, https://doi.org/https://doi.org/10.1016/j.epsl.2014.12.035, 2015.

Pörtner, H.-O., Roberts, D., Masson-Delmotte, V., Zhai, P., Tignor, M., Poloczanska, E., Mintenbeck, K., Alegría, A., Nicolai, M., Okem, A., Petzold, J., Rama, B., and Weyer, N., eds.: IPCC Special Report on the Ocean and Cryosphere in a Changing Climate, Cambridge University
890 Press, Cambridge, UK and New York, NY, USA, https://doi.org/10.1017/9781009157964, 2019.

Pritchard, H. D., Ligtenberg, S. R. M., Fricker, H. A., Vaughan, D. G., van den Broeke, M. R., and Padman, L.: Antarctic ice-sheet loss driven by basal melting of ice shelves, Nature, 484, 502–505, https://doi.org/10.1038/nature10968, 2012.

Reese, R., Winkelmann, R., and Gudmundsson, G. H.: Grounding-line flux formula applied as a flux condition in numerical simulations fails for buttressed Antarctic ice streams, The Cryosphere, 12, 3229–3242, https://doi.org/10.5194/tc-12-3229-2018, 2018.

895 Reese, R., Garbe, J., Hill, E. A., Urruty, B., Naughten, K. A., Gagliardini, O., Durand, G., Gillet-Chaulet, F., Gudmundsson, G. H., Chandler, D., Langebroek, P. M., and Winkelmann, R.: The stability of present-day Antarctic grounding lines – Part 2: Onset of irreversible retreat of Amundsen Sea glaciers under current climate on centennial timescales cannot be excluded, The Cryosphere, 17, 3761–3783, https://doi.org/10.5194/tc-17-3761-2023, 2023.

Rignot, E., Mouginot, J., Morlighem, M., Seroussi, H., and Scheuchl, B.: Widespread, rapid grounding line retreat of Pine Is-
900 land, Thwaites, Smith, and Kohler glaciers, West Antarctica, from 1992 to 2011, Geophysical Research Letters, 41, 3502–3509, https://doi.org/https://doi.org/10.1002/2014GL060140, 2014a.

Rignot, E., Mouginot, J., and Scheuchl, B.: MEaSUREs InSAR-Based Ice Velocity of the Amundsen Sea Embayment, Antarctica, Version 1, Boulder, Colorado USA. NASA National Snow and Ice Data Center Distributed Active Archive Center, https://doi.org/10.5067/MEASURES/CRYOSPHERE/nsidc-0545.001, [Date Accessed: 10/06/21], 2014b.

905 Robel, A. A., Seroussi, H., and Roe, G. H.: Marine ice sheet instability amplifies and skews uncertainty in projections of future sea-level rise, Proceedings of the National Academy of Sciences, 116, 14 887–14 892, https://doi.org/10.1073/pnas.1904822116, 2019.

Rosier, S. H. R., Reese, R., Donges, J. F., De Rydt, J., Gudmundsson, G. H., and Winkelmann, R.: The tipping points and early warning indicators for Pine Island Glacier, West Antarctica, The Cryosphere, 15, 1501–1516, https://doi.org/10.5194/tc-15-1501-2021, 2021.

Sun, S., Cornford, S. L., Liu, Y., and Moore, J. C.: Dynamic response of Antarctic ice shelves to bedrock uncertainty, Cryosphere, 8, 1561–1576,
910   https://doi.org/10.5194/tc-8-1561-2014, 2014.

Wake, L. and Marshall, S.: Assessment of current methods of positive degree-day calculation using in situ observations from glaciated regions,
    Journal of Glaciology, 61, 329–344, https://doi.org/10.3189/2015JoG14J116, 2015.

Wang, Y., Lai, C.-Y., and Cowen-Breen, C.: Discovering the rheology of Antarctic Ice Shelves via physics-informed deep learning,
    https://doi.org/10.21203/rs.3.rs-2135795/v1, 2022.

915 Wang, Y., Zhang, X., Ning, W., Lazzara, M. A., Ding, M., Reijmer, C. H., Smeets, P. C. J. P., Grigioni, P., Heil, P., Thomas, E. R., Mikolajczyk,
    D., Welhouse, L. J., Keller, L. M., Zhai, Z., Sun, Y., and Hou, S.: The AntAWS dataset: a compilation of Antarctic automatic weather station
    observations, Earth System Science Data, 15, 411–429, https://doi.org/10.5194/essd-15-411-2023, 2023.

Wernecke, A., Edwards, T. L., Nias, I. J., Holden, P. B., and Edwards, N. R.: Spatial Probabilistic Calibration of a High-resolution Amundsen
    Sea Embayment Ice Sheet Model with Satellite Altimeter Data, The Cryosphere, 14, 1459–1474, https://doi.org/10.5194/tc-14-1459-2020,
920   2020.